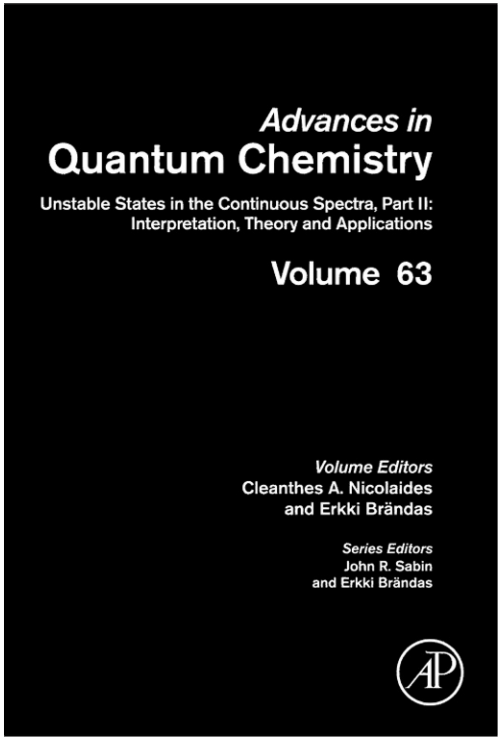




From Vitali Averbukh and Přemysl Kolorenč, Electronic Decay in Multiply Charged Polyatomic Systems.
In: John R. Sabin and Erkki Brändas, Series editors, Advances in Quantum Chemistry, Vol 63.
Unstable States in the Continuous Spectra, Part II: Interpretation, Theory and Applications,
Edited by Cleanthes A. Nicolaides and Erkki Brändas.
San Diego: Academic Press, 2012, pp. 309–342.
ISBN: 978-0-12-397009-1

CHAPTER 6

# Electronic Decay in Multiply Charged Polyatomic Systems

**Vitali Averbukh**[a] and **Přemysl Kolorenč**[b]

Contents



**Abstract** Inner-shell ionization of atoms, molecules, and clusters often leads to creation of highly excited ionic states that are embedded into double (or even multiple) ionization continua and decay by electron emission. The most common electronic decay process triggered by core ionization is known as Auger effect. The dynamics of the Auger decay is usually assumed to be exponential, and the process is characterized by a decay rate. The advent of the high-intensity x-ray free-electron lasers and their envisaged applications in

[a] Department of Physics, Imperial College London, Prince Consort Road, SW7 2AZ London, UK
*E-mail address:* v.averbukh@imperial.ac.uk
[b] Institute of Theoretical Physics, Faculty of Mathematics and Physics, Charles University in Prague, V Holešovičkách 2, 180 00 Prague, Czech Republic
*E-mail address:* kolorenc@mbox.troja.mff.cuni.cz

Advances in Quantum Chemistry, Volume 63
ISSN 0065-3276, DOI: 10.1016/B978-0-12-397009-1.00006-0

molecular imaging have made it necessary to consider Auger-type processes in polyatomic systems under conditions of multiple ionization, both in the core and in the valence shells. Here, we review our recent theoretical work on the theory of electronic decay in multiply charged molecules and clusters. Particular attention is given to the effects of the spectator vacancies on the Auger decay rates, trapping of the Auger electron in a multiply charged system, and collective decay of two vacancies.

## 1. INTRODUCTION

In 1925, Pierre Auger discovered a "compound photoelectric effect" [1] that constituted emission of secondary electrons with kinetic energies independent of the energy of the ionizing photon. This phenomenon, now known as Auger effect [2], is a consequence of the electron-electron interaction in an atom (or a molecule) bearing an inner-shell vacancy. If the energy of the inner-shell-ionized state is higher than the double ionization potential, one of the outer-shell electrons can recombine into the vacant inner-shell orbital (see Figure 6.1) giving another outer-shell electron (Auger electron) enough energy to be ionized. Auger effect is, thus, a basic manifestation of electronic correlation in matter. Since the kinetic energies of the Auger electrons are related to the quantized energies of the singly and the doubly ionized states, they can serve as a fingerprint of a given atom. A small shift of the atomic Auger energies due to the chemical environment (chemical shift) can provide further information on the studied species. This makes Auger electron spectroscopy [2] particularly useful for surface analysis [3].

The first theory of Auger effect was given by G. Wentzel (1927) in his seminal work on nonradiative quantum jumps [4]. Wentzel used hydrogenic bound-state functions and the asymptotic forms of the free electron

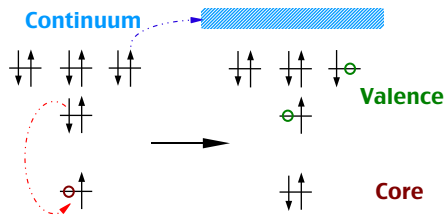


**Figure 6.1** Schematic representation of one of the channels of the $1s^{-1}$ $Ne^{+}$ Auger decay: one of the valence electrons ($2s$) is filling the core vacancy while another one ($2p$) is ejected into continuum. The same final state results also from the $2p \rightarrow 1s$ recombination and $2s$ ionization (not shown here). The former ("direct" ) and the latter ("exchange") contributions interfere due to electron indistinguishability.

waves to predict the order of magnitude of an electronic decay rate in a two-electron system. Adapted to a single Auger decay channel leading to a singlet final state of the dication (see Figure 6.1), Wentzel's expression reads

$$\Gamma = \pi \left| \left\langle \varphi_{\mathrm{val}}(\vec{r}_1)\varphi'_{\mathrm{val}}(\vec{r}_2) \left| \frac{1}{r_{12}} \right| \varphi_{\mathrm{core}}(\vec{r}_1)\varphi_{\varepsilon}(\vec{r}_2) \right\rangle + \left\langle \varphi_{\mathrm{val}}(\vec{r}_1)\varphi'_{\mathrm{val}}(\vec{r}_2) \left| \frac{1}{r_{12}} \right| \varphi_{\mathrm{core}}(\vec{r}_2)\varphi_{\varepsilon}(\vec{r}_1) \right\rangle \right|^2 , \quad (1)$$

It embodies the idea that one of the electrons participating in the Auger transition "jumps" from a valence orbital, $\varphi_{\mathrm{val}}$, to the core orbital, $\varphi_{\mathrm{core}}$, while the second electron is ejected from another valence orbital, $\varphi'_{\mathrm{val}}$, to the continuum with the kinetic energy $\varepsilon$ (cf. Figure 6.1). Electron indistinguishability leads to two interfering pathways for such a jump, often called "direct" and "exchange." Despite the strong approximations used in Wentzel's original theory (e.g., use of very approximate electronic orbitals), it does predict the order of magnitude of the Auger rate almost well (1 $\mathrm{fs}^{-1}$, to be compared with 0.1–0.5 $\mathrm{fs}^{-1}$ for the *K*-shell Auger of second row elements [5]).

Auger decay can be triggered by photoionization of a core electron using x-ray radiation. Recently, new-generation x-ray sources – x-ray free electron lasers (XFELs) – have become available at a number of facilities around the world [6]. These sources are characterized by uncommonly high intensities (up to $\sim 10^{18}$ $\mathrm{W/cm^2}$) and, prospectively, also by very short pulse durations (down to ~1 fs) [6]. This unique characteristics of XFEL radiation led researchers to propose that it can be suitable for imaging of macromolecules in gas phase by single-molecule x-ray diffraction [7]. Significant experimental progress with nanometer-resolution XFEL imaging has been achieved recently [8]. Feasibility of extending this fascinating idea to atomic-resolution measurements depends on the extent of the radiation damage caused by the XFEL radiation. Thus, theoretical simulations of the radiation damage could be very helpful in choosing the optimal pulse characteristics for the envisaged atomic-resolution imaging.

State-of-the-art molecular mechanics simulations of macromolecule–XFEL interaction [7] rely on the classical description of atomic and electronic motion, in combination with quantum-mechanical rates for the electronic processes induced by the high-intensity x-rays. The latter include photoionization, predominantly of inner-shell electrons, and Auger processes following the creation of the corresponding inner-shell vacancies. In the high-intensity regime necessary for obtaining the diffraction picture of a single molecule with atomic resolution, the target species become multiply ionized well within the XFEL pulse duration [7, 9, 10]. It could be expected, therefore, that many of the electronic processes leading to the radiation

damage are modified by the presence of multiple positive charges. Concentrating specifically on the Auger decay, the core hole lifetimes could be affected by additional positive charges residing both on the atom bearing the core vacancy and on the neighboring atoms. Several important aspects make electronic decay in such multiply ionized systems different from the ones in free atoms. First, the rate of the exponential decay in the field of a positive charge (or charges) does not have to match the one in the singly core-ionized molecule. Furthermore, multiple ionization can lead to Auger electrons trapping, changing Auger dynamics qualitatively from exponential to oscillatory one. Finally, a collective decay of two vacancies becomes possible. Here, we review our recent progress in ab initio studies of Auger dynamics under conditions of multiple ionization. The general theoretical framework is given in Section 2. Applications of the ab initio theory to Auger decay in the presence of single or multiple spectator charges are given in Section 3. Several directions for future studies are outlined in Section 4.

## 2. FANO-ADC THEORY OF ELECTRONIC DECAY WIDTHS

Dynamics of the electronic decay in isolated atomic and small molecular systems ionized by low-intensity (e.g., synchrotron) radiation is understood fairly well [2, 11]. At high enough energies of the ionizing photon, the inner-shell ionization event and the decay of the resulting vacancy state can be treated separately, with the latter being described as a nonradiative transition. The concept of sudden ionization and the validity of the two-step description of the Auger transition are discussed, for example, in Refs. [12, 13]. The nonradiative electronic decay process can be treated within a number of theoretical formalisms, including, for example, that of non-Hermitian quantum mechanics [14, 15]. In Auger physics, we are typically dealing with long-lived resonances for which the Fano theory [16, 17] provides a particularly useful theoretical framework. Within this formalism, the nonradiative transition occurs due to coupling between the artificially constructed bound-like state, $\Phi$, describing the inner-shell-ionized system with the energy above the double ionization threshold and the continuum states of the same energy, $\chi_{\beta,\epsilon_\beta}$ describing the doubly ionized system in its $\beta$th state with the energy $E_\beta$ and the emitted Auger electron with kinetic energy $\epsilon_\beta$. In Fano approach, the continuum states $\chi_{\beta,\epsilon_\beta}$ are constructed in such a way that, to a good approximation, they are not coupled by the full Hamiltonian $\hat{H}$:

$$\langle \chi_{\beta',\epsilon'} | \hat{H} | \chi_{\beta,\epsilon} \rangle \approx (E_\beta + \epsilon)\, \delta_{\beta',\beta}\, \delta(E_{\beta'} + \epsilon' - E_\beta - \epsilon)\,. \tag{2}$$

It can be shown [16, 17] that the bound-like state $\Phi$, once prepared, will decay approximately exponentially in time,

$$|\langle\Phi|\Psi(t)\rangle|^2 = e^{-\Gamma t/\hbar}, \quad \Psi(t=0) = \Phi\,, \tag{3}$$

where $\Psi(t)$ is the full wavefunction of the system and the decay rate, $\Gamma/\hbar$, is given through

$$\Gamma = \sum_{\beta=1}^{N_c} \Gamma_\beta = 2\pi \sum_{\beta=1}^{N_c} \left|\langle\Phi|\hat{H} - E_r|\chi_{\beta,\epsilon_\beta}\rangle\right|^2, \tag{4}$$

where $N_c$ is the number of the bound states of the doubly ionized system being energetically lower than the inner-shell-ionized state $\Phi$, or in other words, the number of the open decay channels and $E_r$ is the energy of the decaying state.

For the result (4) to be applicable to the computation of the electronic decay rates, one has to provide sensible approximations for the multi-electron bound ($\Phi$) and continuum ($\chi_{\beta,\epsilon_\beta}$) wavefunctions. In the simplest case of single inner-shell ionization, these are wave functions of a singly ionized $N$-electron system, that is, $(N-1)$-electron states. Such states can be conveniently constructed using the technique of single-ionization algebraic diagrammatic construction (ADC) [18]. The ADC methodology has been originally developed within the Green's function formalism [19]. Here, however, we would like to briefly review the single-ionization ADC from a different standpoint, using the intermediate state representation (ISR) as proposed by Schirmer [20].

Consider the Hartree–Fock (HF) ground state of the $N$-electron neutral cluster, $\Phi_0^N$. One can form a complete orthonormal set of the $(N-1)$-electron basis functions, $\Phi_J^{(N-1)}$, applying the so-called physical excitation operators, $\{\hat{C}_J\}$, to the HF ground state:

$$\Phi_J^{(N-1)} = \hat{C}_J \Phi_0^N, \tag{5}$$
$$\{\hat{C}_J\} \equiv \{c_i;\, c_a^\dagger c_i c_j, i<j;\, c_a^\dagger c_b^\dagger c_i c_j c_k, a<b, i<j<k;\, \ldots\}\,,$$

where $c_i$ and $c_a^\dagger$ are annihilation and creation operators, respectively, the subscripts $i, j, k, \ldots$ relate to the occupied spin-orbitals and the subscripts $a, b, c, \ldots$ relate to the unoccupied spin-orbitals. The basis set (5) is used in the familiar configuration interaction (CI) expansion of the wavefunction. This expansion, once truncated after some specific excitation class [$J$], possesses such important drawbacks as slow convergence and lack of size consistency.

The ADC method overcomes these drawbacks by using a more complicated basis for the expansion of the $(N-1)$-electron wavefunctions. The idea is to apply the physical excitation operators, $\{\hat{C}_J\}$, to the perturbation-theoretically corrected, or "correlated", ground state of the neutral system,

$$\begin{aligned} \Psi_J^0 &= \hat{C}_J \Psi_0^N, \\ \Psi_0^N &= \Phi_0^N + \Psi_0^{(1)} + \Psi_0^{(2)} + \Psi_0^{(3)} + \cdots, \end{aligned} \tag{6}$$

where $\Psi_0^{(n)}$ is the $n$th-order correction to the HF ground state obtained by the standard many-body perturbation theory (see, e.g., Ref. [21]). Unfortunately, the resulting correlated excited states (CESs), $\Psi_J^0$, are not orthonormal. ADC takes care of this problem by orthonormalizing them in two steps to obtain the so-called intermediate states, $\tilde{\Psi}_J$. First, Gram–Schmidt orthogonalization *between the excitation classes* is performed to obtain the "precursor" states, $\Psi_J^\#$:

$$\Psi_J^\# = \Psi_J^0 - \sum_{\substack{K \\ [K]<[J]}} \left\langle \tilde{\Psi}_K | \Psi_J^0 \right\rangle \tilde{\Psi}_K, \tag{7}$$

that is, the functions belonging to the higher [e.g., two-hole, one-particle (2h1p) or $[J]=2$] excitation class are made orthogonal to those of all the lower [in this case, only one-hole (1h) or $[K]=1$] excitation classes. Second, the precursor states are orthonormalized symmetrically *inside each excitation class*:

$$\tilde{\Psi}_J = \sum_{\substack{J' \\ [J']=[J]}} \left( \underline{\underline{\rho}}^{\#-\frac{1}{2}} \right)_{J',J} \tilde{\Psi}_{J'}, \qquad \left( \underline{\underline{\rho}}^{\#} \right)_{J',J} = \langle \Psi_{J'}^\# | \Psi_J^\# \rangle, \tag{8}$$

where $\left( \underline{\underline{\rho}}^{\#} \right)_{J',J}$ is the overlap matrix of the precursor states belonging to the same excitation class. The above two-step procedure can be applied iteratively, noting that the CESs of the lowest (1h) excitation class are by definition also the precursor states. Any state of the $(N-1)$-electron system can be represented using the orthonormal basis of the intermediate states:

$$\Psi_q^{(N-1)} = \sum_i \sum_{[J]=i} Y_{q,J} \tilde{\Psi}_J. \tag{9}$$

The expansion coefficients, $Y_J$, are obtained by the diagonalization of the Hamiltonian matrix constructed in the basis of the intermediate states. It is a crucial feature of the ADC approach that the Hamiltonian matrix elements of the type $\langle \tilde{\Psi}_J | H | \tilde{\Psi}_J \rangle$ can be expressed analytically via the orbital energies and the electron repulsion integrals if one performs the orthonormalization

procedure of Eqs. (7) and (8) approximately and consistently with the order of the many-body perturbation theory, which is used for the construction of the correlated ground state [see Eq. (6)]. Moreover, it can be shown [20] that the truncation of the expansion (9) after the excitation class $[J] = m$ introduces an error of the order of $2m$, which should be compared to $m + 1$ for the slower-converging CI expansion. The accuracy of the expansion in excitation classes (9) should be, of course, consistent with that of the perturbation theoretical series for the correlated ground state (6). Thus, the order, $n$, at which the perturbation theoretical expansion (6) is truncated is the single parameter defining the level of the ADC approximation. For this reason, ADC schemes of various quality are usually denoted as ADC($n$), $n = 2, 3, 4, \ldots$ in full analogy with the well-known MP2, MP3, MP4, ... perturbation-theoretical techniques for the ground state of the neutral system. The ADC(2) scheme for singly ionized states describes the many-electron wavefunctions in the basis of 1h and 2h1p intermediate states treating the coupling between the 1h states and between 1h states and 2h1p states in the second and in the first order, respectively. ADC(2) approximation neglects the coupling between the different 2h1p basis functions. The extended ADC(2) scheme [ADC(2)x] takes into account the coupling between the 2h1p states in the first order (i.e., on CI level). The third-order ADC(3) scheme, while still confined to the basis of 1h and 2h1p intermediate states, treats the coupling between the 1h states and between 1h states and 2h1p states in the third and in the second order, respectively. A detailed description of the single-ionization ADC(2) and ADC(3) schemes, including the expressions for the Hamiltonian matrix elements can be found in Ref. [22]. The proof of the size consistency of the ADC($n$) schemes has been given in Refs. [20]. The main limitation of the existing ADC($n$) schemes is that they are applicable to ionized and/or excited states of closed-shell systems only.

Let us show how the ADC($n$) schemes can be used for the ab initio calculations of the decay rates within Fano formalism. To this end, we need to show that both bound ($\Phi$) and continuum ($\chi_{\beta,\epsilon_\beta}$) $(N-1)$-electron states [see Eq. (4)] can be approximated by the expansion in the basis of the intermediate states (9). In order to describe a perfectly bound state, the wavefunction $\Phi$ must not contain any component corresponding to the possible final states of the decay. These components are to be found among the $m = 2$ (2h1p) and the higher excitation classes. Indeed, the final state of the Auger decay is characterized by two vacancies ("holes") and a single electron in the continuum ("particle") (here we neglect the effect of satellites and double Auger decay [2]). In a simple approximation, the 2h1p configurations corresponding to the open decay channels originate from the $(N-2)$-electron 2h configurations, which are lower in energy than the decaying state:

$$E_{i,j}^{(N-2)} = \langle \Phi_{i,j}^{(N-2)} | H | \Phi_{i,j}^{(N-2)} \rangle < E_\Phi, \quad \Phi_{i,j}^{(N-2)} = c_i c_j \Phi_0^N . \tag{10}$$

Consequently, in order to obtain the ADC($n$) approximation for $\Phi$, one can limit the physical excitation operators used in the construction of the CESs to those which satisfy the appropriate energy criterion:

$$\begin{aligned}\Psi_J^0 &= \hat{C}_J \Psi_0^N, \\ \{\hat{C}_J\} &\equiv \Big\{ c_i;\ c_a^\dagger c_i c_j, i<j, E_{i,j}^{(N-2)} > E_\Phi; \\ &\qquad c_a^\dagger c_b^\dagger c_i c_j c_k, a<b, i<j<k, E_{i,j,k}^{(N-3)} > E_\Phi; \ldots \Big\}.\end{aligned} \tag{11}$$

Similarly, the continuum-like functions, $\chi_{\beta,\epsilon_\beta}$, describing the possible final states of the electronic decay, are naturally found among the ADC($n$) eigenstates of the 2h1p character

$$\chi_{\beta,\epsilon} \sim \Psi_q^{\mathrm{2h1p}} = \sum_i \sum_{[J]=i} Y_{q,J} \tilde{\Psi}_J, \quad 1 - \sum_{[J]=2} |Y_{q,J}|^2 \ll 1 \tag{12}$$

that correspond to the open decay channels. Upon the completion of the selection process, one can construct and diagonalize the initial state and the final state Hamiltonians on the basis of the restricted sets of the intermediate states using the standard methods. The ADC($n$) state approximating the $\Phi$ component can be identified, for example, as the one possessing the maximal overlap with the cluster orbital representing the initial vacancy. Since no configurations corresponding to the open decay channels were used in the ADC-ISR expansion for the bound-like component, $\Phi$, it will be one of the lowest-energy eigenvectors of the ADC Hamiltonian. Therefore, a highly efficient Davidson diagonalization technique [23] can be used to diagonalize the matrix.

Despite the ability of ADC($n$) to produce 2h1p-like wavefunctions in the continuum region of the spectrum, there still exists a major difficulty in associating these ADC($n$) eigenstates with the approximate continuum states of Fano theory. The difficulty stems from the fact that the ADC($n$) calculations, and ab initio quantum chemical calculations in general, are routinely performed using the $\mathcal{L}^2$ bases, usually the Gaussian ones. As a result, the $\mathcal{L}^2$ and not the scattering boundary conditions are imposed and the $\Psi_q^{\mathrm{2h1p}}$ functions are not properly normalized,

$$\langle \Psi_q^{\mathrm{2h1p}} | \Psi_{q'}^{\mathrm{2h1p}} \rangle = \delta_{q,q'} \tag{13}$$

[cf. Eq. (2)]. Moreover, the corresponding eigenenergies, $E_q^{\mathrm{2h1p}}$, are discrete and are not expected to fulfill the energy conservation relation for the non-radiative decay, $E_q^{\mathrm{2h1p}} = E_\Phi$, except by coincidence. An efficient way to deal with the above complications is provided by the computational approach

developed by Langhoff and Hazi and known as Stieltjes-Chebyshev moment theory or Stieltjes imaging [24]. This approach rests in the fact that although decay width (4) cannot be calculated using the discretized continuum functions directly, the spectral moments of Eq. (4) calculated using the pseudospectrum are good approximations to the spectral moments constructed using the true continuum [24]:

$$\sum_{\beta} \int E^k \left| \langle \Phi | H - E_r | \chi_{\beta,\epsilon_\beta} \rangle \right|^2 dE \approx \sum_{q} \left( E_q^{2h1p} \right)^k \left| \langle \Phi | H - E_r | \Psi_q^{2h1p} \rangle \right|^2 . \qquad (14)$$

Using the techniques of moment theory, one can recover the correct value of the decay width (4) from the pseudospectrum through a series of consecutive approximations of increasing order, $n_S$ [24]. Stieltjes imaging has been first applied to the calculation of Auger decay widths by Carravetta and Ågren [25]. A particularly efficient realization of the Stieltjes imaging procedure has been described in detail in Ref. [26]. Standard formulation of the moment theory requires full diagonalization of the final state Hamiltonian matrix, which poses a formidable challenge for polyatomic systems. This computational bottleneck was realized already early on [27], and a number of suggestions as to how it can be overcome exist in the literature [28]. More recently, it has been suggested to use block-Lanczos pseudospectrum, rather than full spectrum, as the input for the Stieltjes imaging procedure [29]. It has been shown that the Lanczos-Stieltjes technique can be used for efficient computation of both intra- and interatomic decay widths [30].

The Fano-ADC technique outlined above can be generalized to the case of multiply ionized systems. Full description of the effect of the additional vacancies requires, of course, an ab initio approach that explicitly takes into account multiple ionization. In the case of a single additional charge, the ADC scheme for doubly ionized states would be appropriate. Such a scheme was developed by Schirmer and Barth [31]. The extended second-order ADC technique for double ionization [31] treats explicitly the two-hole (2h) and the three-hole one-particle (3h1p) excitation classes up to the second and first orders, respectively. Fano-ADC(2)x for decay widths of doubly ionized states embedded into triple ionization continua has been developed in Ref. [32].

## 3. APPLICATIONS OF FANO-ADC THEORY TO AUGER DECAY IN THE MULTIPLY IONIZED SYSTEMS

Let us describe several recent applications of the Fano-ADC theory to Auger decay in multiply ionized systems. We shall start with the simplest problem of this kind – effect of a single neighboring charge on the rate of atomic Auger decay. Then, we shall explore the effect of a spectator vacancy residing

on the core-ionized atom undergoing an Auger transition. Finally, we shall investigate the effect of Auger electron trapping in a multiply ionized cluster.

### 3.1. Auger decay in the field of a positive charge

Suppose an Auger transition occurs in the field of a stationary point charge being at distance $R$ from the core-ionized atom, $R$ being in the order of 1 Å or bigger. In such a case, Wentzel's formula (1) suggests that the Auger rate can be influenced by the charge through the distortions of the electronic orbitals participating in the transition. The tightly bound core orbital, $\varphi_{\text{core}}$, is not likely to be affected, since its binding energy is typically at least two orders of magnitude higher than interaction energy of the core electron with a unit charge at 1 Å distance. Typical kinetic energy of an Auger electron is also much higher than its interaction energy with the point charge. A visible effect of the charge on the Auger rate (1) can come, nevertheless, through distortion of the valence orbitals, $\varphi_{\text{val}}$ and $\varphi'_{\text{val}}$, especially if the latter are easily polarizable. Indeed, binding energies of atomic valence orbitals ranging from ∼3.9 to ∼24.6 eV are of the same order of magnitude as the electron–proton attraction at the distance of 1 Å (∼14.4 eV).

Let us look closer at the possible effect of the point charge on the Auger rate bearing in mind the importance of the valence orbital distortion. To this end, we shall further simplify Wentzel's expression (1) by neglecting the "exchange" and representing the "direct" Auger transition matrix element as a repulsion energy between two charge clouds:

$$V_{\text{Auger}} = \int \mathrm{d}^3 r_1 \int \mathrm{d}^3 r_2 \, \varphi_{\text{val}}(\vec{r}_1)\varphi_{\text{core}}(\vec{r}_1) \, \frac{1}{r_{12}} \, \varphi'_{\text{val}}(\vec{r}_2)\varphi_{\varepsilon}(\vec{r}_2) \tag{15}$$

and using multipole expansion [33]:

$$V_{\text{Auger}} = \sum_{l,m} \left\langle \varphi_{\text{val}}(\vec{r}_1) \left| r_1^l Y_{lm}(1) \right| \varphi_{\text{core}}(\vec{r}_1) \right\rangle \left\langle \varphi'_{\text{val}}(\vec{r}_2) | Y_{lm}(2)/r_2^{l+1} | \varphi_{\varepsilon}(\vec{r}_2) \right\rangle , \tag{16}$$

where $Y_{lm}$ are spherical harmonics as defined in Ref. [33]. Effectively, multipole expansion breaks the two-electron transition into the recombination and the ionization parts. The lowest nonzero angular momentum contribution to the expansion (16) defines the multiplicity of the given Auger transition.

Following Bloch [34], one can perform a crude analysis of Eq. (16) assuming that the recombination matrix element scales as $r_{\text{core}}^l$, where $r_{\text{core}}$ is the spatial extension of the core orbital, while the ionization matrix element scales as $1/r_{\text{val}}^{l+1}$, where $r_{\text{val}}$ is the spatial extension of the valence orbital. Since $r_{\text{core}} \ll r_{\text{val}}$, we obtain

$$V_{\text{Auger}} \sim r_{\text{core}}^l / r_{\text{val}}^{l+1} . \tag{17}$$

Practically, this scaling means that in order to increase the Auger rate, one has to lower the multiplicity of the transition, $l$, and/or to contract the valence orbital. Both these effects can be achieved through valence orbital distortion by the point charge. Indeed, at atom–proton distances larger than $r_{val}$ one can expect orbital distortion to result in the symmetry lowering that naturally leads to the change in Auger transition multiplicity. At shorter distances, a proton penetrating the valence electron cloud would lead to an effective $r_{val}$ smaller than that in a free system. In what follows, we shall explore these effects quantitatively using Fano-ADC theory of the Auger decay widths.

Let us first consider a simple Auger process with only a single decay channel [$N_c = 1$, see Eq. (4)]. Although not characteristic of $K$-shell Auger, such processes take place upon $(n-1)p$ ionization of alkaline earth atoms, for example, in $(2p^{-1})$ $Mg^+$, where the only nonradiative decay pathway involves the two $3s$ electrons: $(2p^{-1})$ $Mg^+ \rightarrow (3s^{-2})$ $Mg^{2+} + e^-$. Assume that $(2p^{-1})$ $Mg^+$ Auger decay occurs in the field of a stationary positive charge, say, of a proton fixed at the distance $R$ from the $Mg^+$ ion. Then, following the arguments given above, we should expect the decay width, $\Gamma$, to vary as a function of $R$ due to distortion of the valence $3s$ orbital. In Figure 6.2 we present the results of our Fano-ADC(2)x calculations for the $\Gamma(R)$ in the $(2p^{-1})$ $Mg^+$–$H^+$ system [35] that indeed reveals such a variation.

At large Mg–proton separations, the Fano-ADC(2)x width converges to about 0.16 meV, in a good agreement with the theoretical value of Walters and Bhalla for the isolated Mg atom (0.145 meV) [36]. Our results show that at the distances below 4 Å, the decay width grows very strongly with decreasing $Mg^+$–$H^+$ distance. Practically, the same result is obtained when removing the Gaussian basis from the proton, that is, the possible transfer of Mg electron density to the neighboring charge does not play a key role in the effect (see Figure 6.2). Moreover, the predicted increase of the decay width is not an artifact of the Gaussian basis set itself that, of course, also changes with $R$ – this is verified by repeating the Fano-ADC(2)x calculation in full Gaussian basis, but with zero charge on the "proton," finally, the clear indication that the predicted effect is due to the distortion of the valence orbital comes from another set of ab initio calculations, in which, we "freeze" the Gaussian orbital coefficients in the Mg $3s$ orbital of Mg–$H^+$ at their values at the largest considered distance of $R = 6.5$ Å. The results presented in Figure 6.2 show that the strong effect of the Auger width increase practically vanishes if the $3s$ orbital is frozen [35].

Further insight into the strong variation of the Auger decay width as a function of the Mg–proton distance is gained by the qualitative analysis in the spirit of Eqs. (16) and (17). Indeed, at $R \rightarrow \infty$ $(2p^{-1})$ $Mg^+$ Auger transition is of dipole–dipole type [$l = 1$, see Eq. (16)]. As the Mg–proton distance decreases, the Mg $3s$ orbital is distorted such that it attains a nonzero $p_z$ component, reducing the multiplicity of the Auger transition to $l = 0$ and leading to the increase in the Auger width. This effect of the valence orbital distortion

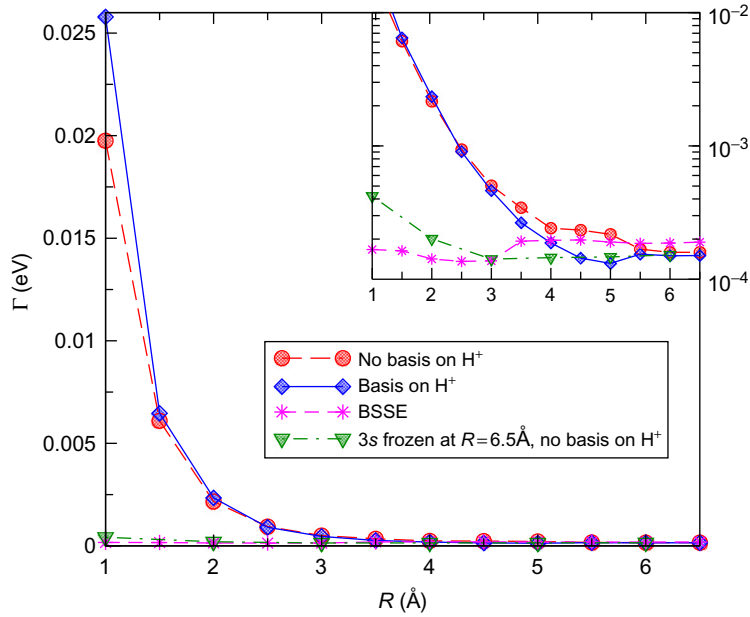


**Figure 6.2** Auger decay width of $(2p_z^{-1})$ $Mg^+$–$H^+$ as a function of the Mg–proton distance, $R$. $z$ is Mg–proton axis. Diamonds and solid line: Fano-ADC(2)x calculation with atomic orbital basis centered both on Mg and on the proton; circles and long-dashed line: Fano-ADC(2)x calculation with atomic orbital basis centered only on Mg; stars and short-dashed line: Fano-ADC(2)x calculation for $(2p_z^{-1})$ $Mg^+$ alone, with atomic orbital basis centered both on Mg and at the distance $R$ along the $z$-axis, showing the so-called basis set superposition error (BSSE); triangles and dashed-dotted line: Fano-ADC(2)x calculation with atomic orbital basis centered on Mg only, with the 3$s$ orbital of Mg being frozen at its shape at $R = 6.5$Å. The inset shows the low-$\Gamma$ part of the plot on logarithmic scale. See Ref. [35] for the details of the computation.

at $R > 2.5$ Å is readily seen in the data presented in Figure 6.3 [panels (a) and (b)]. As the proton approaches the $Mg^+$ ion further, it penetrates the valence electron orbital and eventually leads to its contraction, see Figure 6.3, panel (c). Thus, also at $R > 2.5$ Å, although the distortion of the 3$s$ orbital along the Mg–proton axis decreases, the orbital contraction effect [quantified by decrease of $r_{\rm val}$ – see Eq. (17)] leads to further increase of the Auger rate.

The above analysis suggests that the spectacular effect of the neighboring charge on the single-channel Mg 2$p$ Auger decay has to do with the polarizable Mg 3$s$ orbital that is involved both in the recombination and in the ionization parts of the two-electron transition. Let us consider now a more general situation, in which a polarizable orbital is involved only in the ejection of the Auger electron. An example of such a transition is readily provided by 2$s$-ionized Mg. Indeed, 2$s$ ionization leads to the process in which

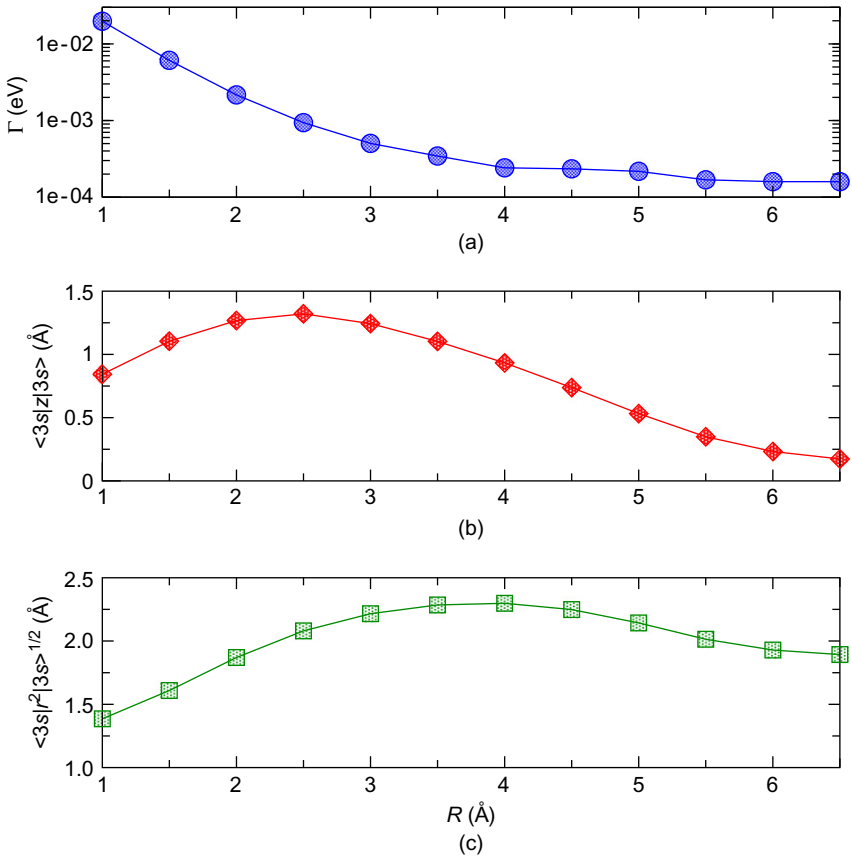


**Figure 6.3** (a) Fano-ADC(2)x result for the Auger decay width of $(2p_z^{-1})$ $Mg^+$–$H^+$ as a function of the Mg–proton distance, *R* (logarithmic scale); (b) *z* expectation value of the Mg 3*s* orbital as a function of the Mg–proton distance, *R*, showing the extent of the orbital distortion along the Mg–proton axis; (c) mean radius of the Mg 3*s* orbital as a function of the Mg–proton distance, *R*, showing the spatial extent. See Ref. [35] for the details of the computation.

one of the 2*p* electrons fills the vacancy while a 3*s* electron is ejected into continuum: $(2s^{-1})$ $Mg^+ \rightarrow (2p^{-1}3s^{-1})$ $Mg^{2+} + e^-$. This decay is characterized by the recombination transition occurring within a single $(n = 2)$ electronic shell and as such belongs to the class of Coster-Kronig (CK) decay processes [2]. The efficient recombination part of the transition and the relatively low kinetic energies of the CK electrons contribute to the typically large widths of the CK decay. In the particular case of $(2s^{-1})$ $Mg^+$, the CK transition is by far the leading decay channel with the competing $(2s^{-1})$ $Mg^+ \rightarrow (3s^{-2})$ $Mg^{2+} + e^-$ Auger decay being much weaker.

Figure 6.4 shows the results of the Fano-ADC(2)x calculation of the $(2s^{-1})$ $Mg^+$ decay width in the $Mg^+$–$H^+$ system as a function of the Mg–proton distance. The decay is completely dominated by the CK process, accounting for 95–99% of the total electronic decay width. At large $R$, the Fano-ADC(2)x result assuming no electron density on the proton is in excellent agreement with the $R$-matrix prediction for bare $(2s^{-1})$ $Mg^+$ [37]. We observe a well-pronounced dependence of the CK on the Mg–proton distance that is drastically reduced by artificially "freezing" the 3$s$ orbital at its large-$R$ shape. The magnitude of the neighboring charge effect is smaller than in the case of the $(2p^{-1})$ $Mg^+$ decay, apparently because the distorted valence orbital is only involved in the ionization part of the two-electron transition. Noteworthy is a clearly distinguishable effect that the electronic density on the proton has on the decay. Allowing part of the electronic density to reside on the proton diminishes the electronic density on the core ionization site and as a result leads to the reduction of the CK decay width (see Figure 6.4).

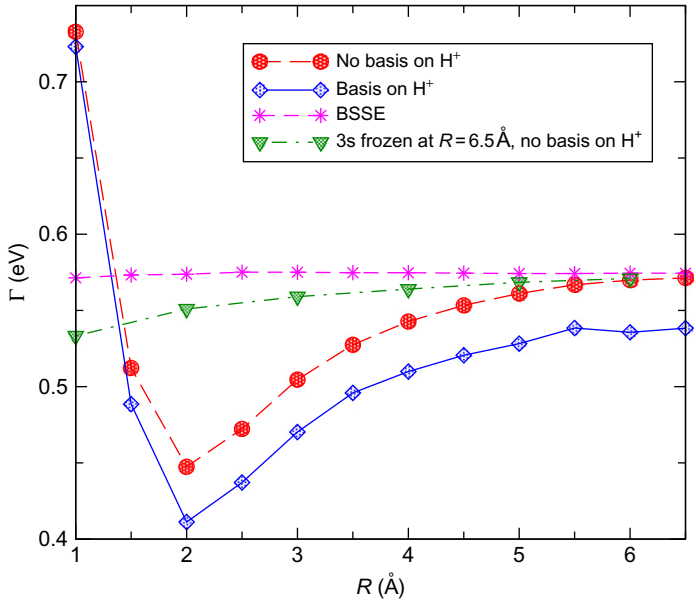


**Figure 6.4** Decay width of $(2s^{-1})$ $Mg^+$–$H^+$ as a function of the Mg–proton distance, $R$. Diamonds and solid line: Fano-ADC(2)x calculation with atomic orbital basis centered both on Mg and on the proton; circles and long-dashed line: Fano-ADC(2)x calculation with atomic orbital basis centered only on Mg; stars and short-dashed line: BSSE (see Figure 6.2); triangles and dashed-dotted line: Fano-ADC(2)x calculation with atomic orbital basis centered on Mg only, with the 3$s$ orbital of Mg being frozen at its shape at $R = 6.5$Å. See Ref. [35] for the details of the computation.

Assuming that the neighboring charge was formed long before an instantaneous Mg core ionization, the physical decay width is produced by the Fano-ADC calculation with basis set on the proton. If, on the other hand, Mg and a neighboring site ionization occur closely in time on the scale of the CK lifetime, the dynamics of the neighboring hole should be taken into account. Such a hole dynamics induced by electron correlation can take place at fixed nuclear geometries on the timescales comparable to the ones of CK or Auger decay [38] and is expected to be strongly influenced by the nuclear motion, at least on a bit longer timescales. Consideration of this effect should be a subject of future studies.

In summary, ab initio results for a number of Auger-type transitions show a pronounced dependence of the Auger width on the atom–proton distance. The origin of this dependence can be traced to the distortion of the outer valence atomic orbital by the field of the proton. A simple qualitative physical picture can be used to explain the Auger rate dependence in terms of the change of multiplicity of Auger transitions and the valence orbital contraction as a result of the interaction with the positive charge. The magnitude of the predicted neighboring charge effect differs substantially between different Auger-type transitions, but is found to be the strongest at the atom–proton distances of about 1–2 Å, that is, at the distances of the order of chemical bond length. At the distances of 3–4 Å, typical of the bond lengths in van der Waals clusters, the neighboring charge effect is much less pronounced.

### 3.2. *K*-shell Auger lifetime variation in doubly ionized Ne and first-row hydrides

Auger decay lifetimes can be affected not only by the additional positive charges residing on neighboring atoms but also by the multiple ionization of the atom bearing the core vacancy. Here, we shall explore the effect of the double ionization of a single atom on the Auger lifetimes. Since the Auger transitions of interest for the radiation damage in single-molecule x-ray diffraction are mainly induced by *K*-shell ionization of C, N, and O atoms, we specifically target doubly (*KK*- and *KL*-) ionized states of $CH_4$, $NH_3$, and $H_2O$ as model systems, comparing them with the corresponding transition in the isoelectronic Ne atom.

Let us first consider Auger processes in doubly ionized Ne as a simple prototype system. Auger-active states of $Ne^{2+}$ can be classified as stemming from $1s^{-2}$, $1s^{-1}2s^{-1}$ and $1s^{-1}2p^{-1}$ configurations. The first one of those, that is, the "hollow atom," has recently been observed in the XFEL studies [39]. Looking at the spectator–core–hole *KK*–*KLL* Auger decay process in the hollow Ne, one immediately notices that it has twice the number of the decay pathways relative to the normal *K*–*LL* Auger transition. In the simplest approximation, one would expect, thus, the *KK*–*KLL* decay rate to be just

twice the *K–LL* one. Further, one notices that a couple of a bit more subtle effects can push the hollow Ne decay rate into opposite directions. First, double *K*-shell ionization leads to contraction of the valence orbitals in the initial state of the process, making the Auger matrix elements larger. Second, the kinetic energy of the *KK–KLL* Auger electrons is a bit higher than that of the *K–LL* (by about 70 eV [40]) ones which could have just the opposite effect. Looking at the theoretical values for the *KK–KLL* widths available in the literature, namely 707 meV (C.P. Bhalla *et al.*, 1973 [41]), 804 meV (M.H. Chen, 1991 [42]), and 623 meV (Pelicon *et al.*, 2001 [43]), one finds that all of them exceed the normal Auger width in Ne (240 meV [5]) by more than twice, suggesting that the effect of the valence orbital contraction is the dominant one. The Voigt fit analysis of a 3 eV wide *KK–KLL* feature in the experimental spectrum [40] supports this conclusion.

In the very recent work [44], the Auger decay widths were calculated using the Fano-ADC method outlined in Section 2. Our Fano-ADC computation for the hollow Ne produces the decay width of 506 meV, which is lower than the available literature values and extremely close to twice the normal Auger width. In fact, it has been found that all the *KK–KLL* decay channels attain about twice as larger partial widths than their *K–LL* counterparts [44]. Noteworthy, our Fano-ADC result for the normal Auger width 251 meV agrees rather well with the recommended literature value [5], and our partial width analysis for the *K–LL* transition is in good correspondence with the available experimental and theoretical results [45] (see Table 6.1). Nevertheless, the discrepancy between our result and the literature values (by themselves having a spread of more than 20%, see Table 6.2) could well result from the underestimation of the very strong relaxation effects in the hollow atom states by the second-order ADC scheme employed in our calculation. We believe that further work on the decay lifetimes of the hollow Ne is needed.

Auger dynamics of a hollow Ne atom presents a particular interest because a three-electron *KK–LLL* process can contribute to the decay of the core vacancies. Such a process, in which two valence electrons recombine into the core orbital to produce an extra-energetic free electron, has been first observed in doubly *L*-shell-ionized Ar atoms [52] and later in Kr and Xe [53]. The corresponding partial decay width in *LL*-ionized Ar was estimated to be in the range of 0.01–1 meV. To our knowledge, there are so far no theoretical or experimental data available for such a three-electron Auger transition in hollow Ne. Our Fano-ADC calculation for the Ne *KK–LLL* process gives the partial decay width of about 0.05 meV, well within the range of the estimated *LL–MMM* Ar values. Assuming that our calculation underestimates the valence orbital contraction effect, this figure presents a lower bound for the three-electron process width. Although clearly negligible relative to the total hollow Ne decay width, the *KK–LLL* process can well be observable, as in the case of heavier rare gas atoms, since it produces highly energetic

**Table 6.1** Comparison of the branching ratios of the *K–LL* Auger transition in singly core-ionized Ne

| $Ne^+$ Transition | | Present | Kelly [46] | Yarzhemsky [45] | Nicolaides1 [47] | Nicolaides2 [48] | Howat1 [49] | Howat2 [49] | Exp. [50, 51] |
|---|---|---|---|---|---|---|---|---|---|
| | $^3P$ | 0.0 | 0.0 | 0.0 | – | – | – | – | – |
| $K–L_{2,3}L_{2,3}$ | $^1D$ | 50.5 | 61.2 | 58.2 | 67.1 | 66.9 | 57.3 | 61.2 | 60.9 |
| | $^1S$ | 9.5 | 9.6 | 10.2 | 5.7 | 4.7 | 9.0 | 9.2 | 9.5 |
| $K–L_1L_{2,3}$ | $^3P$ | 10.6 | 6.1 | 9.3 | 3.5 | 3.8 | 9.6 | 7.8 | 6.3 |
| | $^1P$ | 19.5 | 17.0 | 16.8 | 18.4 | 19.5 | 18.5 | 16.7 | 17.2 |
| $K–L_1L_1$ | $^1S$ | 9.9 | 6.1 | 5.5 | 5.3 | 5.1 | 5.7 | 5.0 | 6.1 |
| **Total width (meV)** | | **251** | **219** | **242** | **227** | **230** | **288** | **244** | **220 ± 30** |

Branching ratios are given in %, the total widths are in meV. Howat1 and Howat2 results correspond to the Hartree–Fock and transition state basis sets of Ref. [49] respectively. The experimental values for *K–LL* transition are taken from Albiez *et al.* [50] (branching ratios) and from Avaldi *et al.* [51] (total width).

**Table 6.2** Comparison of the branching ratios of the *KK–KLL* Auger transitions in doubly core-ionized Ne

| $Ne^{2+}$ Transition | | Present | Pelicon [43] | Chen [42] | Bhalla [41] |
|---|---|---|---|---|---|
| | $^2P$ | 0.0 | 0.3 | 0.4 | |
| $KK - KL_{2,3}L_{2,3}$ | $^2D$ | 59.0 | 49.2 | 44.0 | 66.2 |
| | $^2S$ | 8.1 | 9.2 | 12.6 | |
| $KK - KL_1L_{2,3}$ | $^2P^{(-)}$ | 6.9 | 1.1 | 0.7 | |
| | $^2P^{(+)}$ | 22.6 | 33.0 | 31.6 | 25.0 |
| $KK - KL_1L_1$ | $^2S$ | 3.4 | 7.0 | 10.7 | 7.9 |
| **Total width (meV)** | | **506** | **623** | **805** | **707** |

Branching ratios are given in %, the total widths are in meV.

electrons well outside the energy region of the two-electron transitions. Interestingly, an analogous "collective" interatomic three-electron process can turn out to be the main decay channel in doubly inner-valence-ionized clusters (see Section 3.4 and Ref. [48]).

Going from hollow Ne to core-valence-ionized Ne, one should consider two types of configurations, namely $1s^{-1}2s^{-1}$ and $1s^{-1}2p^{-1}$ ones, which lead to both singlet and triplet states and turn out to have distinctly different patterns of lifetime variation with the spin multiplicity. The results of our Fano-ADC calculations of Auger widths for core-valence-ionized Ne are given in Table 6.3. Looking at the results of these ab initio calculations, one readily notices that while spin multiplicity plays no role for the Auger widths of the $KL_{2,3}$ states, the widths of the $KL_1$ states depend crucially on whether the two holes form a singlet or a triplet. Indeed, the corresponding $^1S$ state decays about 1.6 times faster than the triplet state. The origin of this trend becomes apparent if one looks at the partial widths of the $KL_1$ states (see Table 6.3). In the decay of the singlet initial state, the recombination from 2*s* orbital to 1*s* one is operative and $2s^{-1}\,2p^{-2}$ and $2s^{-2}\,2p^{-1}$ electronic configurations of the $Ne^{3+}$ final states are about evenly populated. In the case of the triplet decaying state, however, the single electron in the 2*s* orbital has the same spin as the one in the 1*s* orbital and, therefore, cannot fill the 1*s* vacancy. The $Ne^{3+}(2s^{-2}\,2p^{-1}\,^2P)$ channel is still accessible but only via higher-order processes comprising three-electron transitions. This leads to a radical drop in efficiency by nearly 90%. This effect fully explains the difference between the total Auger rates for the singlet $^1S$ and triplet $^3S$ initial states. Comparing this situation to the decay of the $KL_{2,3}$ states, one notices that the partial decay widths for the $Ne^{3+}(2s^{-1}\,2p^{-1})$ channels remain more or less unchanged when going from singlet to triplet initial states, up to some redistribution of intensity between different terms of the $2s^{-1}2p^{-2}$ final configuration. In total, the

**Table 6.3** Fano-ADC total and partial Auger decay widths (in meV) for doubly ionized Ne atom

| Final state | $1s^{-1}\,2s^{-1}$ $^1S$ | $1s^{-1}\,2s^{-1}$ $^3S$ | $1s^{-1}\,2p^{-1}$ $^1P$ | $1s^{-1}\,2p^{-1}$ $^3P$ |
|---|---|---|---|---|
| $2p^{-3}\,^4S$ | – | 0 | – | 0 (0) |
| $2p^{-3}\,^2D$ | 0 | 0 | 78 (75) | 77 (76) |
| $2p^{-3}\,^2P$ | 1 | 0 | 31 (37) | 33 (37) |
| $2s^{-1}\,2p^{-2}\,^4P$ | – | 0 | – | 12 (11) |
| $2s^{-1}\,2p^{-2}\,^2D$ | 127 | 135 | 7 (0) | 23 (28) |
| $2s^{-1}\,2p^{-2}\,^2S$ | 16 | 15 | 4 (0) | 6 (6) |
| $2s^{-1}\,2p^{-2}\,^2P$ | 0 | 0 | 53 (52) | 26 (23) |
| $2s^{-2}\,2p^{-1}\,^2P$ | 123 | 16 | 24 (23) | 25 (23) |
| **Total width** | **267** | **166** | **197** (187) | **202** (204) |

Electronic configurations and terms of the decaying states are specified in the first row. The literature values in parentheses are taken from Ref. [55]. See Ref. [44] for the details of the Fano-ADC computation.

**Table 6.4** Comparison of the Fano-ADC results with the available theoretical and experimental values for the *K–LL* Auger decay widths in $CH_4$, $NH_3$, and $H_2O$ molecules

| | Present | Theory | | | Experiment | | | |
|---|---|---|---|---|---|---|---|---|
| $CH_4$ | 85 | [56] 75 | [57] 96 | [58] 96 | [59] $107 \pm 10$ | [60] $120 \pm 10$ | [61] $83 \pm 10$ | [62] $94 \pm 1$ |
| $NH_3$ | 123 | [63] 106 | | | | | | |
| $H_2O$ | 148 | [25] 150 | | | [64] $160 \pm 5$ | | | |

The decay widths are in meV, citations are given in square brackets. Experimental value for ammonia is lacking because of the vibrational broadening in the Auger electron spectrum of ammonia [65]. See Ref. [44] for the details of the Fano-ADC computation.

decay widths of both singlet and triplet $1s^{-1}2p^{-1}$ states are about 80% of the Ne $K-LL$ Auger rate, which is close to what is expected on the basis of the simple counting of the available Auger decay pathways.

Let us now consider the effect of a spectator vacancy on the Auger rate of the C, N, and O core hole in $CH_4$, $NH_3$, and $H_2O$ molecules, respectively. These molecules are isoelectronic with Ne; however, the degeneracy of the outer valence orbitals is preserved only in the tetrahedral $CH_4$. The Fano-ADC Auger widths of the singly core-ionized molecules [44] are presented in Table 6.4 alongside the available literature data. The calculated total Auger

widths for the Auger-active main electronic states of the doubly ionized molecules are given in Table 6.5. The results for the molecular Auger decay widths reveal the trends analogous to the one observed in Ne atom. In particular, it has been found that inner-valence spectator vacancies in methane, ammonia, and water play the same important role as it does in neon: the singlet- to-triplet ratio of the decay widths ranges from 1.6 ($NH_3$, $H_2O$) to 1.8 ($CH_4$). As in the case of Ne atom, this very pronounced difference is due to the fact that the transitions involving inner-valence-core recombination are, at least in the first order of perturbation theory, forbidden in the decay of the triplet states. In the case of outer-valence spectator hole, the effect of the spin multiplicity on the Auger rate is small, beyond the accuracy of our computational method. Furthermore, we find that the Fano-ADC decay widths of the hollow ($1s^{-2}$) molecules is approximately twice larger than the corresponding normal Auger widths, in accordance with the doubling of the available decay pathways. Assuming that our calculation for hollow molecules suffer from underestimation of the relaxation in the initial state in the same way

**Table 6.5** Fano-ADC total Auger decay widths (in meV) for different electronic states of doubly ionized $CH_4$, $H_2O$, and $NH_3$ molecules

| Decaying state | Γ (meV) | Decaying state | Γ (meV) |
|---|---|---|---|
| Ne ($\Gamma_{1s^{-1}} = 251$ meV) | | $CH_4$ ($\Gamma_{1a_1^{-1}} = 85$ meV) | |
| $1s^{-1}\,2p^{-1}\,{}^1P$ | 197 | $1a_1^{-1}\,1t_2^{-1}\,{}^1T_2$ | 68 |
| $1s^{-1}\,2p^{-1}\,{}^3P$ | 202 | $1a_1^{-1}\,1t_2^{-1}\,{}^3T_2$ | 69 |
| $1s^{-1}\,2s^{-1}\,{}^1S$ | 267 | $1a_1^{-1}\,2a_1^{-1}\,{}^1A_1$ | 90 |
| $1s^{-1}\,2s^{-1}\,{}^3S$ | 166 | $1a_1^{-1}\,2a_1^{-1}\,{}^3A_1$ | 49 |
| $1s^{-2}\,{}^1S$ | 506 | $1a_1^{-2}\,{}^1A_1$ | 167 |
| $NH_3$ ($\Gamma_{1a_1^{-1}} = 123$ meV) | | $H_2O$ ($\Gamma_{1a_1^{-1}} = 148$ meV) | |
| $1a_1^{-1}\,3a_1^{-1}\,{}^1A_1$ | 92 | $1a_1^{-1}\,1b_1^{-1}\,{}^1B_1$ | 110 |
| $1a_1^{-1}\,3a_1^{-1}\,{}^3A_1$ | 94 | $1a_1^{-1}\,1b_1^{-1}\,{}^3B_1$ | 116 |
| $1a_1^{-1}\,1e^{-1}\,{}^1E$ | 100 | $1a_1^{-1}\,3a_1^{-1}\,{}^1A_1$ | 121 |
| $1a_1^{-1}\,1e^{-1}\,{}^3E$ | 105 | $1a_1^{-1}\,3a_1^{-1}\,{}^3A_1$ | 118 |
| | | $1a_1^{-1}\,1b_2^{-1}\,{}^1B_2$ | 122 |
| | | $1a_1^{-1}\,1b_2^{-1}\,{}^3B_2$ | 126 |
| $1a_1^{-1}\,2a_1^{-1}\,{}^1A_1$ | 126 | $1a_1^{-1}\,2a_1^{-1}\,{}^1A_1$ | 157 |
| $1a_1^{-1}\,2a_1^{-1}\,{}^3A_1$ | 81 | $1a_1^{-1}\,2a_1^{-1}\,{}^3A_1$ | 99 |
| $1a_1^{-2}\,{}^1A_1$ | 230 | $1a_1^{-2}\,{}^1A_1$ | 311 |

The Fano-ADC Auger decay widths of the single core vacancies are given for each molecule in parentheses. To facilitate the comparison, the Fano-ADC results for Ne atom are also given. See Ref. [44] for the details of the Fano-ADC computation.

as our results for hollow Ne, the true decay rates of the *KK*–*KLL* widths of the first-row hydrides could be about 20% higher than our theoretical predictions.

In summary, the spin state of the two holes has a major effect on the rate of the Auger decay of one-site doubly ionized states. Although singlet core-inner-valence-ionized states decay about as fast as the singly core-ionized ones, their triplet counterparts decay by up to a factor of 1.8 slower. This trend appears to be completely general and is easily explained by spin selection rules. Interestingly, the singlet–triplet factor is largest for methane, which leads one to believe that $sp^3$ hybridized carbon Auger decay in general can proceed significantly slower in the presence of an inner-valence hole. Depending on how probable the inner-valence ionization is for the given experimental conditions, this effect can have significant implications on the timescale of the Auger dynamics in multiply ionized biomolecules.

### 3.3. Suppression of exponential Auger decay in multiply charged systems

Up to now, we have considered the effect of an additional positive charge on the rate of the exponential Auger decay of a core vacancy. Interestingly, the Auger dynamics can change qualitatively in a highly ionized system. Under conditions of multiple ionization, the kinetic energy of the Auger electron may not suffice for leaving the system and the electron will be trapped by the field of the positive charges surrounding the inner-shell-ionized atom [66]. On a more formal level, the final states of the decay, $\chi_{\beta,\epsilon}$, around the resonance energy, $E_r$, will no longer form a continuum, but will rather turn into closely spaced bound states. An electron occupying one of such states will be delocalized across the whole system, yet, will not be able to leave it. With discrete final states, however, one cannot expect the familiar notion of the exponential decay to remain valid and the very basics of our understanding of electronic decay dynamics should be reconsidered. Indeed, a trapped (e.g., Auger) electron can participate in an "inverse Auger" process, that is, it can fill one of the vacancies created by the Auger transition, giving a core electron enough energy to be promoted to another vacancy of the Auger final state. Therefore, the survival probability of the core hole state [see Eq. (3)] can exhibit oscillatory rather than exponential character. This situation is formally similar to the one encountered in the nonradiative decay of excited electronic molecular states due to vibronic coupling. The reason is that the final states of this type of nonradiative decay in molecules can be bound vibrational states of a lower-energy electronic state, that is, not a continuum. For the idealized Bixon–Jortner model assuming uniform energy spacing between the adjacent final states, $\varepsilon$, and uniform initial–final states coupling [67], one can show that the exponential decay persists for times of the order of $\hbar/\varepsilon$. Of course, such a model could be hardly applicable to the

complicated many-electron states involved in the electronic decay. The essential open question is therefore: Can electronic decay processes in a highly charged environment be characterized, even approximately, by exponential dynamics?

In Ref. [68], the character of the electronic decay dynamics in a multiply charged system was investigated by constructing a simple but realistic model based on the $L_1$–$L_{2,3}M$ CK decay in Ar (see Ref. [69] and references therein). Due to the relatively low energy of the recombination transition within a single shell, CK processes are characterized by the emission of relatively slow electrons with kinetic energies of the order of several tens of electron volt. This circumstance makes CK decay processes in general and the Ar $L_1$–$L_{2,3}M$ decay in particular very well suited for the study of the effect of Auger electron trapping by neighboring charges. Indeed, consider an Ar cluster, for example, $Ar_{13}$, interacting with an intense XFEL radiation. Neutral $Ar_{13}$ in its ground state has an icosahedral ($I_h$) equilibrium geometry with the central Ar surrounded by 12 symmetry-equivalent peripheral Ar atoms [70]. Simulations of $Ar_{13}$–XFEL interaction [10] show that one could easily reach a situation where all the Ar atoms in the cluster are singly ionized well before the cluster geometry suffers a significant distortion. Imagine, for simplicity, that the central atom of $Ar_{13}$ is ionized in its 2*s* subshell while the 12 surrounding Ar atoms bear either 2*p* or outer-shell vacancies. Such a distribution of vacancies among the electronic shells is not implausible given that the photoionization cross sections of the outer shell and 2*p* electrons of Ar are higher than that of the 2*s* electron [71]. With the lifetime of about 0.3 fs [69], CK decay of the 2*s* vacancy is more than an order of magnitude faster than Auger decay of $(2p^{-1})$ $Ar^+$ [69, 72]. The timescale for the second ionization of one of the Ar atoms in the case of a long ($\sim$100 fs) XFEL pulse is controlled by the pulse intensity and can be in the range between 10 and 100 fs [10]. For these reasons, we assume the vacancy states of the 12 Ar atoms surrounding the 2*s*-ionized one to be stationary on the time scale of the CK process. If, nevertheless, the Auger decay or a second photoionization event occurs, it would effectively increase the positive charge of the cluster and lead to a stronger trapping of the would-be CK electron.

The kinetic energies of the CK electrons generated by the $L_1$–$L_{2,3}M$ decay in isolated $(2s^{-1})$ $Ar^+$ vary between about 29 and 47 eV [69]. In a multiply ionized $Ar_{13}$ cluster, the energies of the corresponding final doubly ionized states of the central Ar will be elevated (relative to an isolated Ar) by the energy of the interaction of the additional central charge with the 12 peripheral ones. In the simple point-charge approximation, this energy elevation is given by $\Delta E = 12/R_{eq}$, where $R_{eq}$ is the equilibrium central–peripheral atom distance in the neutral $Ar_{13}$. With $R_{eq} = 6.96$ a.u. [70], $\Delta E$ turns out to be just enough to put all the $(2p^{-1}3l^{-1})$ $Ar^{2+}(Ar^+)_{12}$ states of the cluster above the energy of the initial 2*s* vacancy. Hence, as long as the ionized cluster does

not expand, the CK electron that left the central Ar will always be bound to the cluster as a whole. In what follows, we would like to study the implication of the CK electron trapping in $(2s^{-1})$ $Ar^+(Ar^+)_{12}$ on the dynamics of the electronic decay process modeling the peripheral Ar ions by point charges (protons).

In Ref. [68], the initial and the final states of the CK decay in $2s^{-1}$ $Ar^+(H^+)_{12}$ were calculated according to the Fano-ADC scheme (11,12):

$$\Phi = a_{2s}\tilde{\Psi}_{2s} + \sum_{jka} b^a_{jk}\tilde{\Psi}^a_{jk}, \tag{18}$$

$$\chi_n = \sum_{j'k'a'} c^{a'(n)}_{j'k'}\tilde{\Psi}^{a'}_{j'k'},$$

where the possible pairs of the $j,k$ indices are restricted to the doubly ionized configurations with energies higher than that of $\Psi_{2s}$, while the possible pairs of the $j',k'$ indices are restricted to doubly ionized configurations with energies lower than that of $\Psi_{2s}$, that is, to the open channels of the CK transition in an isolated Ar. With the initial and final states of the nonradiative transition specified, we obtain the evolution of the initial state by propagating it in time under the Fano type Hamiltonian, $\hat{H}$, built in the basis of $\{\Phi, \chi_n\}$:

$$\Psi(t) = e^{-i\hat{H}t/\hbar}\Phi, \quad \hat{H} = |\Phi\rangle E_\Phi\langle\Phi| + \sum_n |\chi_n\rangle E_n\langle\chi_n| + (|\Phi\rangle\gamma_n\langle\chi_n| + \text{c.c.}), \tag{19}$$

where the initial–final coupling matrix elements are given by $\gamma_n = \langle\Phi|\hat{H}|\chi_n\rangle$.

The survival probability of the $2s$ vacancy state of the central Ar atom in the model $Ar_{13}$ cluster obtained using Eqs. (3) and (19) (see Figure 6.5) shows a roughly exponential dynamics on the short time scale. During the initial 0.7 fs, the population of the $2s$ vacancy state exhibits oscillations superimposed over exponential decay with the mean rate being very close to the one of the $L_1$–$L_{2,3}M$ transition in an isolated Ar. A striking change of behavior occurs, however, at $t > 0.7$ fs, where even the approximately exponential decay pattern is suppressed completely by an oscillatory one. During this phase of the time evolution, the $2s$ vacancy population rises roughly from 1% to 10% in a clear manifestation of a partial "inverse Auger" transition and then falls back. At later times, the calculated survival probability keeps oscillating within a similar range. Our assumption that surrounding vacancies are stationary limits, however, the validity of the present calculation to times smaller than the Ar $L_{2,3}$–$MM$ Auger life time of $t = 3.7$ fs. Another insight into the mechanism of the exponential decay suppression comes from the examination of the properties of the many-electron wavefunction, $\Psi(t)$, for example, of $\langle\Psi(t)|r^2|\Psi(t)\rangle$ (see Figure 6.1b). In Figure 6.5,

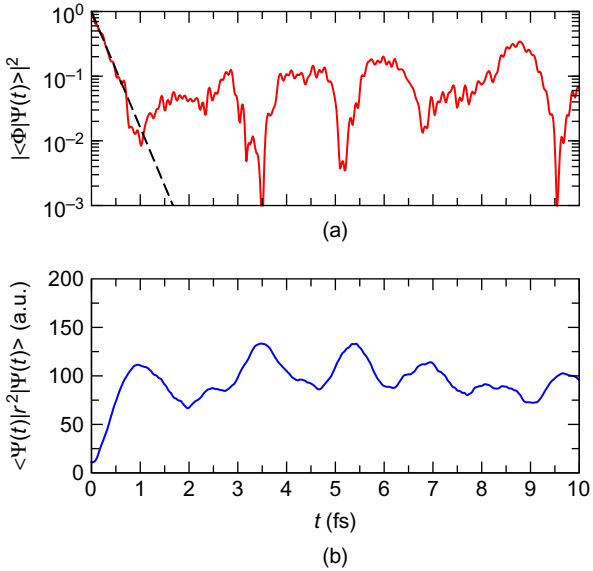


**Figure 6.5** (a) Solid line: survival probability of the 2*s* vacancy in $Ar^+(H^+)_{12}$ plotted on the logarithmic scale. Dashed line: same for the exponential decay of the 2*s* vacancy in an isolated $Ar^+$. (b) Time dependence of the $r^2$ expectation value measuring the spatial extension of the $Ar^+(H^+)_{12}$ electronic wavefunction. See Ref. [68] for the details of the computation.

one can easily notice that the plots of the spatial extent of $\Psi(t)$ and of the survival probability of the 2*s* vacancy state behave as mirror images of each other with the minima of the former corresponding to the maxima of the latter. This suggests the following simple physical picture of the predicted Auger oscillations. The Auger electron wave packet emitted by the central ion is reflected back by the charged cluster potential, leading to peaks of $\langle r^2\rangle(t)$ (Figure 6.5). Propagating back toward the central atom, the Auger electron partly recombines in an inverse Auger transition leading to the partial revivals of $|\langle\Phi|\Psi(t)\rangle|^2$ (Figure 6.5).

In summary, the dynamics of the electronic decay of inner-shell vacancies in a charged environment, such as created by interaction of a cluster with a high intensity FEL radiation, can be qualitatively different from the one induced by a low-intensity source. If the emitted electrons are slow enough to be trapped by the neighboring charges, the familiar exponential decay will be suppressed by quantum beats between the initial state and the quasi-continuum of discrete final states. Physically, the predicted oscillations correspond to creation of the initial vacancy due to the reflections of the emitted electron by the charged cluster potential and the subsequent inverse Auger transition.

### 3.4. Collective interatomic decay of multiple vacancies in clusters

In the above example, we have considered a situation where the presence of additional positive charges leads to suppression of electronic decay through channel closing. It would be tempting to ask whether the reverse physical situation is possible, that is, whether multiple ionization can lead to channel opening resulting in a decay process that occurs exclusively in a multiply inner-shell-ionized system. In fact, an example of such a process, that is, *KK–LLL* decay has been already mentioned in connection with double-core ionization (see Section 3.2). There, however, a collective decay of two core holes is completely overwhelmed by the much more probable normal Auger decay. A recent theoretical work [54] shows that an analogous interatomic collective process can be the dominant decay pathway in doubly ionized clusters.

Interatomic Coulombic decay (ICD) is an electronic decay process that is particularly important for those inner-shell or inner-subshell vacancies that are not energetic enough to give rise to Auger decay. Typical examples include inner-valence-ionized states of rare gas atoms. In isolated systems, such vacancy states are bound to decay radiatively on the nanosecond timescale. A rather different scenario is realized whenever such a low-energy inner-shell-ionized species is let to interact with an environment, for example, in a cluster. In such a case, the existence of the doubly ionized states with positive charges residing on two different cluster units leads to an interatomic (or intermolecular) decay process in which the recombination part of the two-electron transition takes part on one unit, whereas the ionization occurs on another one. ICD [73–75] is mediated by electronic correlation between two atoms (or molecules). In clusters of various sizes and compositions, ICD occurs on the timescale from hundreds of femtoseconds [18] down to several femtoseconds [76–79].

Consider now an inner-shell vacancy state that is not energetic enough to decay by either Auger or ICD mechanisms. Such are, for example, $ns^{-1}$ states of $Ar^+$, $Kr^+$, and $Xe^+$, either isolated or in an environment of other rare gas atoms. Consider further two such vacancy states, say, in a Kr cluster or, a bit more generally, in a mixed Kr/X cluster, where X is another atom or molecule. Neither of the vacancies can decay by electron emission because the energy provided by the $4p \rightarrow 4s$ recombination is not sufficient for $4p$ ionization of either $Kr^+$ (as needed for Auger decay) or a neutral Kr (as needed for ICD). However, if two $4s$-ionized kryptons recombine simultaneously, the released energy would be enough to ionize X:

$$(4s^{-1}, 4s^{-1})(Kr^+)_2X \rightarrow 2\,(4p^{-1})Kr^+ + X^+ + e^- . \qquad (20)$$

A schematic representation of such a collective decay process, or collective ICD (CICD), is given in Figure 6.6. Simple energy considerations imply that,

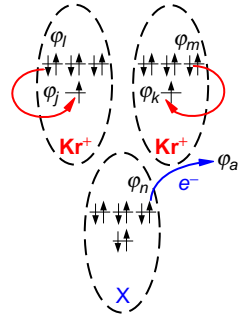


**Figure 6.6** Schematic representation of collective interatomic decay of two inner-shell vacancies, see Eq. (20).

in general, the collective decay occurs without facing a competition from the ICD if $1.5 < (E_{\rm iv} - E_{\rm c})/E_{\rm ion} < 2$, where $E_{\rm iv}$ is the inner valence ionization energy of the given species, $E_{\rm c}$ is the energy of Coulombic repulsion between two singly ionized atoms or molecules (typically 3–4 eV at the equilibrium distances of neutral van der Waals clusters) and $E_{\rm ion}$ is the single ionization energy.

Some qualitative understanding of the CICD can be gained by means of Wentzel-type theory that treats the initial and final states of the decay as single Slater determinants taking electronic repulsion responsible for the transitions as a perturbation. The collective decay of two inner-shell vacancies (see Figure 6.6) is a three-electron transition mediated by two-electron interaction. Thus, the process is forbidden in the first-order perturbation theory, and its rate cannot be calculated by the first-order expressions, such as (1). Going to the second-order perturbation theory, the expression for the collective decay width can be written as

$$\Gamma = 2\pi \left| \sum_i \frac{\langle f|\hat{V}|i\rangle\langle i|\hat{V}|0\rangle}{E_0 - E_i} \right|^2 \delta(E_f - E_0), \quad \hat{V} = \sum_{p<q} \frac{e^2}{r_{pq}}. \tag{21}$$

Here, $|0\rangle$ is the initial doubly inner-shell-ionized [($N$-2)-electron two-hole (2h)] state that can be derived from the $N$-electron HF ground state of the neutral system, $|\Phi_0^{\rm HF}\rangle$, by the application of the annihilation operators, $|0\rangle = \hat{c}_j\hat{c}_k|\Phi_0^{\rm HF}\rangle$, $|f\rangle$ is a final state of the three-hole-one-particle (3h1p) type, $|f\rangle = \hat{c}_a^\dagger\hat{c}_l\hat{c}_m\hat{c}_n|\Phi_0^{\rm HF}\rangle$, and $|i\rangle$'s are the intermediate states. The $\delta$-function of the final–initial energy difference in Eq. (21) reflects the conservation of energy in the course of the nonradiative transition.

Equation (21) suggests that the CICD rate is formed by a superposition of interfering decay pathways, each of which is defined by an intermediate state, $|i\rangle$. Further analysis shows that such states can be either of 2h or of 3h1p type. Consider, for example, $|i\rangle = \hat{c}_l\hat{c}_m|\Phi_0^{\rm HF}\rangle$, where $\hat{c}_{l,m}$ correspond to the

Kr outer-shell vacancies present in the final state, $|f\rangle$. Physically, this means that the three-electron transition consists of virtual two-electron recombination on krypton cations followed by ionization of X (see Figure 6.6). The corresponding recombination matrix element entering Eq. (21) is

$$\begin{aligned}\langle i|V|0\rangle &= \langle \Phi_0^{\mathrm{HF}} \hat{c}_m^\dagger \hat{c}_l^\dagger |\hat{V}| \hat{c}_j \hat{c}_k \Phi_0^{\mathrm{HF}}\rangle \\ &= \langle \varphi_l(\vec{r}_1)\varphi_m(\vec{r}_2)|1/r_{12}|\varphi_k(\vec{r}_1)\varphi_j(\vec{r}_2)\rangle - \langle \varphi_l(\vec{r}_1)\varphi_m(\vec{r}_2)|1/r_{12}|\varphi_j(\vec{r}_1)\varphi_k(\vec{r}_2)\rangle,\end{aligned} \tag{22}$$

where the electron repulsion matrix elements involve the outer-shell ($\varphi_{l,m}$) and the inner shell ($\varphi_{j,k}$) of the Kr's. Assuming that $\varphi_{j,l}$ are localized on the left Kr while $\varphi_{k,m}$ belong to the right Kr (see Figure 6.6), we can obtain the dependence on the recombination matrix element on the interatomic distance, $R_{\mathrm{Kr-Kr}}$, in the limit of large Kr–Kr separation:

$$\begin{aligned}\langle i|V|0\rangle &\approx -\langle \varphi_l(\vec{r}_1)\varphi_m(\vec{r}_2)|1/r_{12}|\varphi_j(\vec{r}_1)\varphi_k(\vec{r}_2)\rangle \\ &\approx -\frac{1}{R_{\mathrm{Kr-Kr}}^3}\langle \varphi_l(\vec{r}_1)|e\vec{r}_1|\varphi_j(\vec{r}_1)\rangle \cdot \langle \varphi_m(\vec{r}_1)|e\vec{r}_2|\varphi_k(\vec{r}_1)\rangle,\end{aligned} \tag{23}$$

where we have neglected the exchange contribution that decreases exponentially with $R_{\mathrm{Kr-Kr}}$ and approximated the direct integral by the leading (dipole–dipole) term of the multipole expansion. The last expression suggests an appealing physical interpretation of the collective decay at large internuclear distances as a two-virtual-photon transition with the two dipole matrix elements in Eq. (23) being regarded as two virtual photons that are "emitted" by the $Kr^+$'s and "absorbed" by X. Within this simple picture, the CICD is analogous to multi-photon transition while Auger decay and ICD are analogous to a single-photon transition.

Proceeding with the large-$R$ analysis of the ionization matrix element, $\langle f|\hat{V}|i\rangle$, we find that at large $Kr_2$–X separations it decreases as $1/R_{\mathrm{Kr_2-X}}^2$. As a result, the contribution of the two-electron recombination – ionization pathway to the decay width depends on the cluster geometry as $1/R_{\mathrm{Kr-Kr}}^6 R_{\mathrm{Kr_2-X}}^4$. Since the decomposition of the $(Kr^+)_2X$ cluster along the $Kr^+$–$Kr^+$ coordinate automatically means elongation of the $Kr_2$–X distance as well, the power law exponents are effectively summed, resulting in the $1/R_{\mathrm{Kr-Kr}}^{10}$ dependence. A detailed analysis shows that this type of power law is characteristic of all the possible decay pathways.

Quantitative results for the collective interatomic decay in $(4s^{-1}, 4s^{-1})$ $(Kr^+)_2Ar$ have been obtained in Ref. [54] using Fano-ADC theory. The results for $\Gamma$ as a function of the Kr–Kr distance (at $R_{\mathrm{Kr_2-Ar}}^{\mathrm{eq}} = 3.3$Å [54]) are shown in Figure 6.7a. At the equilibrium Kr–Kr distance ($R_{\mathrm{Kr_2}}^{\mathrm{eq}} = 4.0$Å [54]), the collective decay width reaches 1.9 meV for triplet and 2.0 meV for singlet doubly ionized states, which corresponds to lifetimes around 300 fs. The predicted lifetime is *five orders of magnitude* shorter than the one of the

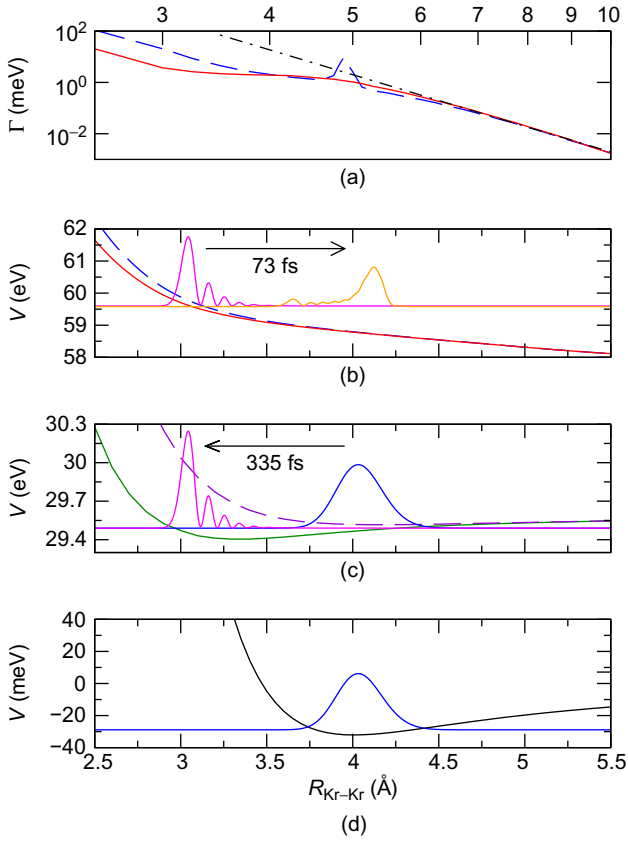


**Figure 6.7** (a) Collective decay widths of $(4s^{-1}, 4s^{-1})$ $(Kr^+)_2Ar$ as functions of $R_{Kr-Kr}$ at $R^{eq}_{Kr_2-Ar} = 3.3$Å. Solid line: triplet, dashed line: singlet, dashed-dotted line: $1/R^{10}$ fit (please, note the doubly logarithmic scale). (b) PESs of $(4s^{-1}, 4s^{-1})$ $(Kr^+)_2Ar$ states, cut at $R^{eq}_{Kr_2-Ar} = 3.3$Å. Solid line: triplet state, dashed line: singlet state. Shown also is the vibrational wave packet promoted from the $(4s\sigma_u^{-1})$ state of $(Kr_2)^+Ar$ [see panel (c)] at the moment of closest approach of the two kryptons, $t_{min} = 335$ fs, and 73 fs later. Direction of motion of the wave packet is shown by an arrow. (c) PESs of $(4s\sigma_{g,u}^{-1})$ $(Kr_2)^+Ar$ states, cut at $R^{eq}_{Kr_2-Ar} = 3.3$Å. Solid line: ungerade state, dashed line: gerade state. Shown also is the vibrational wave packet promoted from the ground state [see panel (d)] at $t = 0$ (right) and at $t_{min}$ (left). Direction of motion of the wave packet is shown by an arrow. (d) PES of the neutral $(Kr_2)Ar$, cut at $R^{eq}_{Kr_2-Ar} = 3.3$Å. Shown also is the vibrational ground state.

radiative decay [54], which means that the process is not suppressed by photon emission. At Kr–Kr separation above 6 Å, the collective decay width shows the predicted $1/R^{10}$ behavior (see Figure 6.7a).

The CICD rate as a function of the Kr–Kr distance was used in the nuclear wave packet simulation of the process within the Born–Oppenheimer picture

[54]. The relevant cuts of the $Kr_2Ar$ potential energy surfaces (PESs) at the symmetric geometry with $R_{Kr_2-Ar}$ frozen at its equilibrium value are shown in Figure 6.7. It is assumed that in the beginning the cluster is in its ground vibrational state. At some later time, 4*s* photoionization occurs on the Kr atoms due to the interaction with the high-intensity FEL beam. The double photoionization can occur either directly by a "vertical," that is instantaneous transition to the $(4s^{-1}, 4s^{-1})$ $(Kr^+)_2Ar$ PES or in two stages, bringing the cluster first onto a $(Kr_2)^+Ar$ PES and only later (by another vertical transition) to a doubly ionized PES (see Figure 6.7). The important difference between the one-step and the two-step processes is that the former creates a vibrational wave packet centered around the equilibrium distance of the neutral ($R_{Kr-Kr} = 4.0$Å), while in the latter process the wave packet created on the singly ionized PES can evolve before being promoted to the repulsive decaying state. If at the first stage of the sequential process the $(4s)\,\sigma_u$ orbital of $Kr_2$ is ionized, the resulting vibrational motion can explore the region of much smaller Kr–Kr distances than in the case of the one-step double ionization. Thus, two-step ionization process, in particular the one proceeding via $(4s)\sigma_u$ ionization, leads the system to the region of much higher collective decay widths than the one-step double ionization and is expected to give a higher yield of the electronic decay. Nuclear dynamics simulations have shown that the CICD yields in the case of one-step double photoionization are 31% and 38% (for triplet and singlet doubly ionized states, respectively), whereas for the two-step ionization into the singlet state, the electronic decay yield reaches 65% [54]. Thus, the nuclear dynamics simulations show that the CICD process can compete successfully with the disintegration of the doubly ionized cluster.

## 4. OUTLOOK

The results presented in this overview point at the significant impact of the charged environment on the Auger-type processes in polyatomic systems. The specific effects of the additional charges on the decay of inner-shell-ionized species range from strong modulation of the exponential decay rate to transition to nonexponential dynamics (in the case of channel closing) or, on the contrary, onset of exponential electronic (nonradiative) decay (in the case of channel opening). The initial work presented here is nothing but a first step toward systematic exploration of this new inner-shell physics. Let us outline a few directions that we think will be most relevant for the future ab initio studies.

On the methodology side, it would be important to generalize the Fano-ADC theory of Section 2 to the case of triple ionization using the second-order ADC scheme of Ref. [80]. Moreover, the problem of different level of treatment of adjacent excitation classes within the existing ADC

schemes deserves some attention. Indeed, normal Auger dynamics can be formally regarded as a transition between 1h and 2h1p states, which are described by us at the moment up to second and first orders, respectively. A balanced description would mean a more accurate (second-order) treatment of 2h1p's. This would require formulation of a new type of ADC schemes in which the adjacent excitation classes are treated up to the same order. Finally, the Fano-type computational approach presented here is by no means limited to the ADC ab initio methodology. An immediate idea would thus be to construct the analogous schemes based on the equation of motion coupled cluster (EOMCC) methods [81]. This could be particularly relevant for treatment of inner-shell ionization of open-shell systems, for which the EOMCC methods have been developed [82].

As far as physical applications go, Auger-type processes in multiply ionized "building blocks" of biomolecules are the immediate target of the theory with the aim to provide an accurate input for the molecular dynamics simulations of the radiation damage. Besides the *K–LL* Auger in C, N, and O atoms in charged environment, the effect of inner-shell ionization of heavier atoms, such as S, on the radiation damage would be very interesting to explore. The higher-order physical processes involving more than a single participator vacancy, such as collective decay, are extremely interesting from the physical point of view, and their role in molecular inner-shell physics is yet to be understood. Moreover, the effect of charged environment on the ICD rates is yet to be investigated. Finally, it is important to take into account the effect of the ionizing field itself, going beyond sudden ionization paradigm and exploring the processes that are forbidden without the presence of the external field, such as laser-enabled Auger decay [83].

## ACKNOWLEDGMENTS

P. K. acknowledges the financial support from the Czech Science Foundation (grant GAČR 202/09/0786) and from the Institutional research plan MSM0021620860. V. A. thanks J.-M. Rost and U. Saalmann for fruitful collaboration on some of the subjects covered in this review. V. A. acknowledges the financial support of the Max Planck Institute for the Physics of Complex Systems (Dresden, Germany) and of the EPSRC (UK) through the Career Acceleration Fellowship (award PHQL_P21289).

## REFERENCES

[1] P. Auger, Sur l'effet photoélectrique composé, J. de Phys. 6 (1925) 205.
[2] W. Mehlhorn, Auger-electron spectrometry of core levels of atoms, in: B. Crasemann (Ed.), Atomic Inner-Shell Physics, Plenum, New York, 1985.
[3] N.H. Turner, J.A. Schreifels, Surface analysis: X-ray photoelectron spectroscopy and Auger electron spectroscopy, Anal. Chem. 72 (2000) 99.
[4] G. Wentzel, Über strahlunglose quantensprünge, Zeits. f. Physik 43 (1927) 524.

[5] J.L. Campbell, T. Papp, Widths of the atomic K - N7 levels, At. Data Nucl. Data Tables 77 (2001) 1.
[6] J. Feldhaus, J. Arthur, J.B. Hastings, X-ray free-electron lasers, J. Phys. B 38 (2005) S799; Y. Ding, A. Brachmann, F.-J. Decker, D. Dowell, P. Emma, J. Frisch, S. Gilevich, G. Hays, Ph. Hering, Z. Huang, R. Iverson, H. Loos, A. Miahnahri, H.-D. Nuhn, D. Ratner, J. Turner, J. Welch, W. White, J. Wu, Measurements and simulations of ultralow emittance and ultrashort electron beams in the linac coherent light source, Phys. Rev. Lett. 102 (2009) 254801; T. Tanaka, T. Shintake, (Eds.), *SPring-8 Compact SASE Source Conceptual Design Report*, RIKEN (2005); M. Altarelli et al., (Eds.), *Technical Design Report*, DESY-2006-097 (2007).
[7] R. Neutze, R. Wouts, D. van der Spoel, E. Weckert, J. Hajdu, Potential for biomolecular imaging with femtosecond X-ray pulses, Nature 406 (2000) 752; R. Neutze, G. Huldt, J. Hajdu, D. van der Spoel, Potential impact of an X-ray free electron laser on structural biology, Rad. Phys. Chem. 71 (2004) 905.
[8] H.N. Chapman et al., Femtosecond X-ray protein nanocrystallography, Nature 470 (2011) 73; M.M. Seibert et al., Single mimivirus particles intercepted and imaged with an X-ray laser, Nature 470 (2011) 78.
[9] H.M. Quiney, K.A. Nugent, Biomolecular imaging and electronic damage using X-ray free-electron lasers, Nat. Phys. 7 (2011) 142.
[10] U. Saalmann, J.M. Rost, Ionization of clusters in strong X-ray laser pulses, Phys. Rev. Lett. 89 (2002) 143401.
[11] H. Ågren, A. Cesar, C.-M. Liegener, Theory of molecular Auger spectra, Adv. Quant. Chem. 23 (1992) 1.
[12] B.T. Pickup, On the theory of fast photoionization processes, Chem. Phys. 19 (1977) 193.
[13] O. Gunarsson, K. Schönhammer, Dynamical theory of Auger processes, Phys. Rev. B 22 (1980) 3710.
[14] N. Moiseyev, Non-Hermitian Quantum Mechanics, Cambridge University Press, Cambridge, UK, 2011.
[15] R. Santra, L.S. Cederbaum, Non-Hermitian electronic theory and applications to clusters, Phys. Rep. 368 (2002) 1.
[16] U. Fano, Effects of configuration interaction on intensities and phase shifts, Phys. Rev. 124 (1961) 1866.
[17] T. Åberg, G. Howat, Theory of Auger effect, in: W. Mehlhorn (Ed.), Corpuscles and Radiation in Matter, Handbuch der Physik, Vol. 31, Springer, Berlin, 1982.
[18] V. Averbukh, L.S. Cederbaum, Ab initio calculation of interatomic decay rates by a combination of the Fano ansatz, Green's-function methods, and the Stieltjes imaging technique, J. Chem. Phys. 123 (2005) 204107.
[19] J. Schirmer, L.S. Cederbaum, O. Walter, New approach to the one-particle Green's function for finite Fermi systems, Phys. Rev. A 28 (1983) 1237; L.S. Cederbaum, Greens functions and propagators for chemistry, in: P.v.R. Schleyer, P.R. Schreiner, N.A. Allinger, T. Clark, J. Gasteiger, P. Kollman, H.F. Schaefer III (Eds.), Encyclopedia of Computational Chemistry, Wiley, New York, 1998.
[20] J. Schirmer, Closed-form intermediate representations of many-body propagators and resolvent matrices, Phys. Rev. A 43 (1991) 4647; F. Mertins, J. Schirmer, Algebraic propagator approaches and intermediate-state representations. I. The biorthogonal and unitary coupled-cluster methods, Phys. Rev. A 53 (1996) 2140; A.B. Trofimov, J. Schirmer, Molecular ionization energies and ground- and ionic-state properties using a non-Dyson electron propagator approach, J. Chem. Phys. 123 (2005) 144115.
[21] A. Szabo, A.S. Ostlund, Modern Quantum Chemistry: Introduction to Advanced Electronic Structure Theory, Dover, New York, 1996.
[22] J. Schirmer, A.B. Trofimov, G. Stelter, A non-Dyson third-order approximation scheme for the electron propagator, J. Chem. Phys. 109 (1998) 4734.
[23] E. Davidson, The iterative calculation of a few of the lowest eigenvalues and corresponding eigenvectors of large real-symmetric matrices, J. Comp. Phys. 17 (1975) 87.

[24] P.W. Langhoff, Stieltjes-Tchebycheff moment-theory approach to molecular photoionization studies, in: T. Rescigno, V. McKoy, B. Schneider (Eds.), Electron-Molecule and Photon-Molecule Collisions, Plenum, New York, 1979; A.U. Hazi, Stieltjes-moment-theory technique for calculating resonance widths, in: T. Rescigno, V. McKoy, B. Schneider (Eds.), Electron-Molecule and Photon-Molecule Collisions, Plenum, New York, 1979.
[25] V. Carravetta, H. Ågren, Stieltjes imaging method for molecular Auger transition rates: Application to the Auger spectrum of water, Phys. Rev. A 35 (1987) 1022.
[26] F. Müller-Plathe, G.H.F. Diercksen, Molecular photoionization cross sections by moment theory. An introduction, in: S. Canuto, J. D'Albuquerque e Castro, F.J. Paixão (Eds.), Electronic Structure of Atoms, Molecules and Solids, World Scientific, Singapore, 1990; F. Müller-Plathe, G.H.F. Diercksen, Perturbative-polarization-propagator study of the photoionization cross section of the water molecule, Phys. Rev. A 40 (1989) 696.
[27] R.K. Nesbet, Stieltjes imaging method for computation of oscillator-strength distributions for complex atoms, Phys. Rev. A 14 (1976) 1065.
[28] V.V. Ivanov, A.V. Luzanov, Semiempirical and ab initio calculations of the full configuration interaction using iterated Krylovs spaces, J. Struct. Chem. 38 (1997) 10; H. Ågren, V. Carravetta, H.J.Aa. Jensen, P. Jørgensen, J. Olsen, Multiconfiguration linear-response approaches to the calculation of absolute photoionization cross sections: HF, $H_2O$, and Ne, Phys. Rev. A 47 (1993) 3810; V. Carravetta, Y. Luo, H. Ågren, Accurate photoionization cross sections of diatomic molecules by multi-configuration linear response theory, Chem. Phys. 174 (1993) 141.
[29] K. Gokhberg, V. Vysotskiy, L.S. Cederbaum, L. Storchi, F. Tarantelli, V. Averbukh, Molecular photoionization cross sections by Stieltjes-Chebyshev moment theory applied to Lanczos pseudospectra, J. Chem. Phys. 130 (2009) 064104.
[30] S. Kopelke, K. Gokhberg, L.S. Cederbaum, F. Tarantelli, V. Averbukh, Autoionization widths by Stieltjes imaging applied to Lanczos pseudospectra, J. Chem. Phys. 134 (2011) 024106; S. Kopelke, K. Gokhberg, V. Averbukh, F. Tarantelli, L.S. Cederbaum, Ab initio interatomic decay widths of excited states by applying Stieltjes imaging to Lanczos pseudospectra, J. Chem. Phys. 134 (2011) 094107.
[31] J. Schirmer, A. Barth, Higher-order approximations for the particle-particle propagator, Z. Phys. A 317 (1984) 267.
[32] P. Kolorenč, V. Averbukh, K. Gokhberg, L.S. Cederbaum, Ab initio calculation of interatomic decay rates of excited doubly ionized states in clusters, J. Chem. Phys. 129 (2008) 244102.
[33] P. M. Morse, H. Feshbach, Methods of Theoretical Physics, McGraw-Hill, New York, 1953.
[34] F. Bloch, Double electron transitions in X-ray spectra, Phys. Rev. 48 (1935) 187.
[35] V. Averbukh, U. Saalmann, J.-M. Rost, Auger decay in the field of a positive charge, submitted to Phys. Rev. A.
[36] D.L. Walters, C.P. Bhalla, Nonrelativistic Auger rates, X-ray rates, and fluorescence yields for the 2p shell, Phys. Rev. A 4 (1971) 2164.
[37] A.G. Kochur, D. Petrini, E.P. da Silva, 2s-photoionisation of atomic magnesium: Shake processes and Coster-Kronig radiationless decay, A&A 365 (2001) 248.
[38] J. Breidbach, L.S. Cederbaum, Migration of holes: Formalism, mechanisms, and illustrative applications, J. Chem. Phys. 118 (2003) 3983; A.I. Kuleff, J. Breidbach, L.S. Cederbaum, Multielectron wave-packet propagation: General theory and application, J. Chem. Phys. 123 (2005) 044111.
[39] L. Young et al., Femtosecond electronic response of atoms to ultra-intense X-rays, Nature 466 (2010) 56; J. Wark, Atomic physics: X-ray laser peels and cores atoms, Nature 466 (2010) 35.
[40] S.H. Southworth, E.P. Kanter, B. Krässig, L. Young, G.B. Armen, J.C. Levin, D.L. Ederer, M.H. Chen, Double K-shell photoionization of neon, Phys. Rev. A 67 (2003) 062712.
[41] C.P. Bhalla, N.O. Folland, M.A. Hein, Theoretical K-shell Auger rates, transition energies, and fluorescence yields for multiply ionized neon, Phys. Rev. A 8 (1973) 649.

[42] M.H. Chen, Auger transition rates and fluorescence yields for the double-K-hole state, Phys. Rev. A 44 (1991) 239.
[43] P. Pelicon, I. Čadež, M. Žitnik, Ž. Šmit, S. Dolenc, A. Mühleisen, R.I. Hall, Formation of the hollow $1s^0\ ^1S$ state of $Ne^{2+}$ by electron impact: Observation by means of an Auger hypersatellite, Phys. Rev. A 62 (2000) 022704.
[44] P. Kolorenč, V. Averbukh, J. Chem. Phys. 135 (2011) 134314.
[45] V.G. Yarzhemsky, A. Sgamellotti, Auger rates of second-row atoms calculated by many-body perturbation theory, J. Elec. Spec. Rel. Phen. 125 (2002) 13.
[46] H.P. Kelly, K Auger rates calculated for $Ne^+$, Phys. Rev. A 11 (1975) 556.
[47] C.A. Nicolaides, Th. Mercouris, Y. Komninos, Many-electron theory of autoionizing states using complex coordinates: The position and the partial and total widths of the $Ne^+$ 1*s* hole state, Int. J. Quantum Chem. 26 (1984) 1017.
[48] C. A. Nicolaides, Th. Mercouris, Partial widths and interchannel coupling in autoionizing states in terms of complex eigenvalues and complex coordinates, Phys. Rev A 32 (1985) 3247.
[49] G. Howat, T. Åberg, O. Goscinski, Relaxation and final-state channel mixing in the Auger effect, J. Phys. B 11 (1978) 1575.
[50] A. Albiez, M. Thoma, W. Weber, W. Mehlhorn, KL2,3 ionization in neon by electron impact in the range 1.550 keV: Cross sections and alignment, Z. Phys. D 16 (1990) 97.
[51] L. Avaldi, G. Dawber, R. Camilloni, G.C. King, M. Roper, M.R.F. Siggel, G. Stefani, M. Zitnik, A. Lisini, P. Decleva, Measurement of Ne 1*s* and 1*snl* satellite photoelectron spectra near threshold, Phys. Rev. A 51 (1995) 5025.
[52] V.V. Afrosimov, Yu.S. Gordeev, A.N. Zinov'ev, D.Kh. Rasulov, A.P. Shergin, Observation of new types of Auger transitions in atoms with two internal vacancies, JETP Lett. 21 (1975) 249.
[53] I. Lee, R. Wehlitz, U. Becker, M. Ya. Amusia, Evidence for a new class of many-electron Auger transitions in atoms, J. Phys. B 26 (1993) L41.
[54] V. Averbukh, P. Kolorenč, Collective interatomic decay of multiple vacancies in clusters, Phys. Rev. Lett. 103 (2009) 183001.
[55] N.M. Kabachnik, J. Tulkki, H. Aksela, S. Ricz, Coherence and correlation in the anisotropy of Ne KL-LLL satellite Auger decay, Phys. Rev. A 49, 4653 (1994).
[56] E. Hartmann, X-ray fluorescence yields for light emitter atoms: Carbon, J. Phys. B 21 (1988) 1173.
[57] M. Coville, T.D. Thomas, Molecular effects on inner-shell lifetimes: Possible test of the one-center model of Auger decay, Phys. Rev. A 43 (1991) 6053.
[58] F.P. Larkins, Influence of core hole screening on molecular Auger rates and inner-shell lifetimes, J. Electron Spectrosc. Relat. Phenom. 67 (1994) 159.
[59] L. Asplund, U. Gelius, S. Hedman, K. Helenelund, K. Siegbahn, P.E.M. Siegbahn, Vibrational structure and lifetime broadening in core-ionised methane, J. Phys. B 18 (1985) 1569.
[60] P.A. Heimann, L.J. Medhurst, M.R.F. Siggel, D.A. Shirley, C.T. Chen, Y. Ma, F. Sette, Zero electron kinetic energy photoemission of $CH_4$ and $CD_4$ at the carbon K ionization threshold, Chem. Phys. Lett. 183 (1991) 234.
[61] H.M. Köppe, B.S. Itchkawitz, A.L.D. Kilcoyne, J. Feldhaus, B. Kempgens, A. Kivimäki, M. Neeb, A.M. Bradshaw, High-resolution C 1*s* photoelectron spectra of methane, Phys. Rev. A 53 (1996) 4120.
[62] T.X. Carroll, N. Berrah, J. Bozek, J. Hahne, E. Kukk, L.J. Sæthre, T.D. Thomas, Carbon 1*s* photoelectron spectrum of methane: Vibrational excitation and core-hole lifetime, Phys. Rev. A 59 (1999) 3386.
[63] F.P. Larkins, L.C. Tulea, E.Z. Chelkowska, Auger electron spectra of molecules: The first row hydrides, Aust. J. Phys 43 (1990) 625.
[64] R. Sankari, M. Ehara, H. Nakatsuji, Y. Senba, K. Hosokawa, H. Yoshida, A. De Fanis, Y. Tamenori, S. Aksela, K. Ueda, Vibrationally resolved O 1*s* photoelectron spectrum of water, Chem. Phys. Lett. 380 (2003) 647.

[65] R.W. Shaw Jr., J.S. Chen, T.D. Thomas, Auger spectrum of ammonia, J. Elec. Spec. Rel. Phen. 11 (1977) 91; J.M. White, R.R. Rye, J.E. Houston, Experimental Auger electron spectrum of ammonia, Chem. Phys. Lett. 46 (1977) 146; R. Camilloni, G. Stefani, A. Giardini-Guidoni, The measured Auger electron spectrum of ammonia vapour, Chem. Phys. Lett. 50 (1977) 213.
[66] C. Gnodtke, U. Saalmann, J.M. Rost, Ionization and charge migration through strong internal fields in clusters exposed to intense x-ray pulses, Phys. Rev. A 79 (2009) 041201(R).
[67] M. Bixon, J. Jortner, Intramolecular radiationless transitions, J. Chem. Phys. 48 (1967) 715.
[68] V. Averbukh, U. Saalmann, J.M. Rost, Suppression of exponential electronic decay in a charged environment, Phys. Rev. Lett. 104 (2010) 233002.
[69] T. Kylli, J. Karvonen, H. Aksela, A. Kivimäki, S. Aksela, R. Camilloni, L. Avaldi, M. Coreno, M. de Simone, R. Richter, K.C. Prince, S. Stranges, $L_1$–$L_{2,3}M$ Coster-Kronig transitions in argon, Phys. Rev. A 59 (1999) 4071.
[70] D.J. Wales et al., The Cambridge Cluster Database, 2007, http://www-wales.ch.cam.ac.uk/CCD.html. A. Cuccoli, A. Macchi, V. Tognetti, R. Vaia, Monte Carlo computations of the quantum kinetic energy of rare-gas solids, Phys. Rev. B 47 (1993) 14923.
[71] D.A. Verner, D.G. Yakolev, I.M. Band, M.B. Trzhaskovskaya, Subshell photoionization cross sections and ionization energies of atoms and ions from He to Zn, At. Data Nucl. Data Tabl. 55 (1993) 233.
[72] J.C. Fuggle, S.F. Alvarado, Core-level lifetimes as determined by x-ray photoelectron spectroscopy measurements, Phys. Rev. A 22 (1980) 1615.
[73] L.S. Cederbaum, J. Zobeley, F. Tarantelli, Giant intermolecular decay and fragmentation of clusters, Phys. Rev. Lett. 79 (1997) 4778.
[74] S. Marburger, O. Kugeler, U. Hergenhahn, T. Möller, Experimental evidence for interatomic Coulombic decay in Ne clusters, Phys. Rev. Lett. 90 (2003) 203401.
[75] T. Jahnke, A. Czasch, M.S. Schöffler, S. Schössler, A. Knapp, M. Käsz, J. Titze, C. Wimmer, K. Kreidi, R.E. Grisenti, A. Staudte, O. Jagutzki, U. Hergenhahn, H. Schmidt-Böcking, R. Dörner, Experimental observation of interatomic Coulombic decay in neon dimers, Phys. Rev. Lett. 93 (2004) 163401.
[76] G. Öhrwall, M. Tchaplyguine, M. Lundwall, R. Feifel, H. Bergersen, T. Rander, A. Lindblad, J. Schulz, S. Peredkov, S. Barth, S. Marburger, U. Hergenhahn, S. Svensson, O. Björneholm, Femtosecond interatomic Coulombic decay in free neon clusters: Large lifetime differences between surface and bulk, Phys. Rev. Lett. 93 (2004) 173401.
[77] R. Santra, J. Zobeley, L.S. Cederbaum, Electronic decay of valence holes in clusters and condensed matter, Phys. Rev. B 64 (2001) 245104.
[78] N. Vaval, L.S. Cederbaum, Ab initio lifetimes in the interatomic Coulombic decay of neon clusters computed with propagators, J. Chem. Phys. 126 (2007) 164110.
[79] V. Averbukh, L.S. Cederbaum, Interatomic electronic decay in endohedral fullerenes, Phys. Rev. Lett. 96 (2006) 053401.
[80] A. Tarantelli, L.S. Cederbaum, Approximation scheme for the three-particle propagator, Phys. Rev. A 46 (1992) 81.
[81] J. Geersten, M. Rittby, R.J. Bartlett, The equation-of-motion coupled-cluster method: Excitation energies of Be and CO, Chem. Phys. Lett. 164 (1989) 57; D.C. Comeau, R.J. Bartlett, The equation-of-motion coupled-cluster method. Applications to open- and closed-shell reference states, Chem. Phys. Lett. 207 (1993) 414.
[82] M. Włoch, J.R. Gour, K. Kowalski, P. Piecuch, Extension of renormalized coupled-cluster methods including triple excitations to excited electronic states of open-shell molecules, J. Chem. Phys. 122 (2005) 214107.
[83] P. Ranitovic, X.M. Tong, C.W. Hogle, X. Zhou, Y. Liu, N. Toshima, M.M. Murnane, H.C. Kapteyn, Laser-enabled Auger decay in rare-gas atoms, Phys. Rev. Lett. 106 (2011) 053002; X.M. Tong1, P. Ranitovic, C.W. Hogle, M.M. Murnane, H.C. Kapteyn, N. Toshima, Theory and experiment on laser-enabled inner-valence Auger decay of rare-gas atoms, Phys. Rev. A 84 (2011) 013405.